

# Effect of SiCw Whiskers on the indentation thermal shock resistance of ZrB<sub>2</sub>-MoSi<sub>2</sub> Composites

Tanay Rudra Paul

NIT-Durgapur: National Institute of Technology Durgapur

Manas Kumar Mondal

NIT-Durgapur: National Institute of Technology Durgapur

Manab Mallik (✉ [manabmallik@gmail.com](mailto:manabmallik@gmail.com))

NIT-Durgapur: National Institute of Technology Durgapur

---

## Research Article

**Keywords:** Borides, whisker, thermal shock, stress intensity

**Posted Date:** June 16th, 2021

**DOI:** <https://doi.org/10.21203/rs.3.rs-612369/v1>

**License:** © ⓘ This work is licensed under a Creative Commons Attribution 4.0 International License.

[Read Full License](#)

---

# Effect of SiC<sub>w</sub> Whiskers on the indentation thermal shock resistance of ZrB<sub>2</sub>-MoSi<sub>2</sub> Composites

Tanay Rudra Paul, Manas Kumar Mondal and Manab Mallik\*

Department of Metallurgical and Materials Engineering,  
National Institute of Technology, Durgapur - 713209, INDIA

## \*Corresponding Author:

Dr. Manab Mallik  
Assistant Professor  
Department of Metallurgical and Materials Engineering  
National Institute of Technology  
Durgapur-713209, India  
Mobile No: +91-9434789014  
Fax: +91-343-2547375  
Email: manabmallik@gmail.com

## Abstract

A comparative evaluation of the thermal shock resistance (TSR) of ZrB<sub>2</sub>-20 MoSi<sub>2</sub>-20 SiC<sub>w</sub> (ZMS<sub>w</sub>20) and ZrB<sub>2</sub>-20 MoSi<sub>2</sub> - 5SiC<sub>w</sub> (ZMS<sub>w</sub>5) composites were studied using the indentation quench method. High-dense ZrB<sub>2</sub> based composites were prepared by multi-stage spark plasma sintering at 1700 °C. The results show that the ZMS<sub>w</sub>20 composite expressed superior crack shielding and TSR under quenching circumstances. The critical temperature differential  $\Delta T_c$  of ZMS<sub>w</sub>20 ceramic ( $\Delta T_c=800^\circ\text{C}$ ) was higher than that of ZMS<sub>w</sub>5 ceramic ( $\Delta T_c=600^\circ\text{C}$ ). The significant enhancement in TSR was imposed residual stresses that improved the resistance to crack progression during thermal shock. Furthermore, an increment in silicon carbide content reduces the crack growth, and increases the TSR of the composites.

**Keywords:** Borides; whisker; thermal shock; stress intensity

## 1. Introduction

During re-entry at the earth atmosphere, leading edges and nose cones of the hypersonic vehicle are encountered in thermal and oxidation loads, leading to the evaporation of the sharp outer surface by aerodynamic heating [1,2]. Moreover, hypersonic velocity also generates shock waves in front of the vehicle [3]. Hence, it is demanded to develop thermal protection system (TPS) materials for overcoming those problems. The TPS materials should have a high melting point, adequate ablation, erosion, and oxidation resistance [4,5]. Therefore, the development of such material is a real challenge. Ultra-high-temperature ceramics (UHTCs) are one of the most favorable high-temperature materials for overcoming these problems. Borides, carbides, and nitrides of early transition metals are considered UHTCs [6-8]. In the group of all ultra-high-temperature ceramics, zirconium diboride ( $ZrB_2$ ) is a suitable material due to it has a very superior melting temperature ( $3250\text{ }^\circ\text{C}$ ) and lower density ( $6.01\text{ g/cm}^3$ ) than other UHTCs [5]. However, zirconium diboride is one of the strong covalent bonds with a hexagonal crystal system [9]. Moreover, the boride ceramics show higher thermal and electrical conductivity at room temperature than nitride and carbide ceramics [8, 10-14]. Borides also have good chemical resistance [8]. So, those unique characteristics of mechanical, physical, and thermal properties make the  $ZrB_2$  ceramic suitable for thermal protection and propulsion systems of hypersonic vehicles, rockets, and other high-temperature industrial fields such as foundry electrodes for electric arc furnace and refractory fields [15,16]. However, the pure monolithic  $ZrB_2$  can not be used in actual application due to its low oxidation resistance and damage tolerance. It is also difficult to fabricate due to its poor self-diffusivity and strong atomic bond strength [17]. Also, a very high temperature (around  $1900^\circ\text{C}$ ) is required for sintering during the pressure-assisted

sintering technique to eliminate the porosity [8]. However, the densification, mechanical properties, oxidation resistance, creep, wear, and ablation resistance of diborides can be enhanced by the addition of the second phase additives like SiC, MoSi<sub>2</sub>, Si<sub>3</sub>N<sub>4</sub>, and tantalum compounds [18-28]. Moreover, SiC and MoSi<sub>2</sub> are the most promising second phase element in ZrB<sub>2</sub> ceramic to achieve a unique combination of mechanical, physical, thermal, and high-temperature oxidation properties [29,30]. Monteverde [29] reported superior sinterability, mechanical, and oxidation behaviors of ZrB<sub>2</sub>-SiC-MoSi<sub>2</sub> composites than the monolithic ZrB<sub>2</sub> and ZrB<sub>2</sub>-SiC composites.

In another work, Mashhadi et al. [18] observed an enhanced density, hardness, and fracture toughness of the ZrB<sub>2</sub>-SiC-MoSi<sub>2</sub> ceramics as compared to ZrB<sub>2</sub>-SiC composites. Guo et al. found that [31] the fracture toughness of ZrB<sub>2</sub>-MoSi<sub>2</sub> ceramics decline with MoSi<sub>2</sub> content, but the superior fracture toughness was observed in the case of ZrB<sub>2</sub> based composite containing 40 vol. % MoSi<sub>2</sub>. They also observed multiple cracking in MoSi<sub>2</sub> of ZrB<sub>2</sub>-40 vol. % MoSi<sub>2</sub> composite. The composite was developed via a hot-pressing technique. During cooling from the pressing temperature lot of residual stresses are developed in MoSi<sub>2</sub> for the reason of the difference in coefficient of thermal expansion of ZrB<sub>2</sub> and MoSi<sub>2</sub>. As a result, the MoSi<sub>2</sub> experiences tensile stress, whereas ZrB<sub>2</sub> is under compressive stress. Therefore, the residual tensile stress in MoSi<sub>2</sub> grains increases with an increase in MoSi<sub>2</sub> concentration. This led to the development of multiple cracks in MoSi<sub>2</sub>, thus ZrB<sub>2</sub>- 40 vol. % MoSi<sub>2</sub> showed superior fracture toughness.

Moreover, numerous authors have been investigated the influences of whiskers silicon carbide (SiCw) on the mechanical properties of ZrB<sub>2</sub> composites [32-34]. Furthermore, Li et al. [35] determined the fracture toughness of the highly-dense ZrB<sub>2</sub> -15 vol.% SiCw (whiskers) - MoSi<sub>2</sub> composites through the single-edged notch beam (SENB)

mode. They concluded that the fracture toughness of the ceramics improved with increasing MoSi<sub>2</sub> concentration and rising the sintering temperature. The fracture toughness reached maximum once specimen densified at 1800 °C, and the measured fracture toughness was close to a specimen that sintered at 1750 °C for the same composition of the composite. Moreover, at the same sintering temperature, the fracture toughness of ZrB<sub>2</sub> -15 vol.% SiC<sub>w</sub> (whiskers) – 15 vol.% MoSi<sub>2</sub> ceramic was close to the fracture toughness of ZrB<sub>2</sub> -15 vol.% SiC<sub>w</sub> (whiskers) – 15 vol.% MoSi<sub>2</sub> composite. Finally, they concluded that ZrB<sub>2</sub> -15 vol.% SiC<sub>w</sub> (whiskers) – 15 vol.% MoSi<sub>2</sub> composites provided the best fracture toughness (5.52±0.03) when sintering was done at 1750 °C because this sample had record level density, lesser grain size, and intergranular fracture.

Researchers have been trying to developing new thermal shock inhibitors of ZrB<sub>2</sub>-based UHTCs ceramics. Less number literature is obtainable on the ZrB<sub>2</sub>-MoSi<sub>2</sub>-SiC<sub>w</sub> ceramics densified by a multi-stage SPS sintering technique. However, the addition of the silicon carbide whisker (SiC<sub>w</sub>) on the thermal shock characteristic of the ZrB<sub>2</sub>-MoSi<sub>2</sub> ceramic is unexplored. The thermal shock resistance characteristic investigation will director the applied application of SiC<sub>w</sub> added ZrB<sub>2</sub>-MoSi<sub>2</sub> based composites. Therefore, the primary objective of this investigation is to identify the role of silicon carbide whisker content on the TSR of ZrB<sub>2</sub>-MoSi<sub>2</sub> ceramics.

## **2 Experimental**

### **2.1 Composite preparation**

High purity (≥99%) raw powders used in the investigation were ZrB<sub>2</sub>, SiC<sub>w</sub> whiskers, and MoSi<sub>2</sub> powder collected from Alfa Aesar, MA, USA. Two ZrB<sub>2</sub>-20 vol.% MoSi<sub>2</sub> based ceramics improved with 5/20 SiC<sub>w</sub> (ZMS<sub>w</sub>5 and ZMS<sub>w</sub>20) were fabricated by multi-stage spark plasma sintering. The procedure had been described in the previous

article [36] in detail. The graphical representation of the multi-stage SPS sintering schedule is presented in Fig.1.

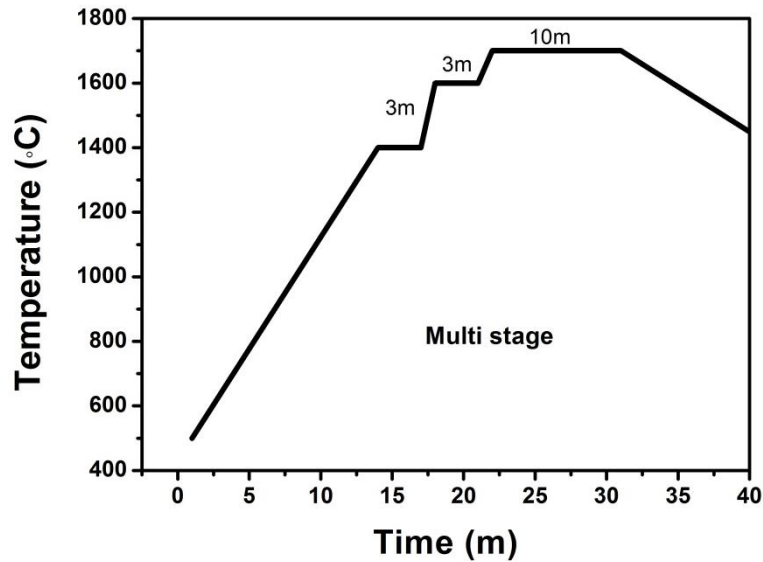


**Fig. 1.** Graphical representation of the multistage SPS sintering heating cycle.

## 2.2 Composite characterization

X-ray diffractometer (XRD) analyses using Cu  $K_{\alpha}$  radiation were performed to identify the existent phases in the sintered composites [37]. The densities of the sintered samples were measured on the basis of the Archimedes principle. Sintered samples were partitioned for microstructure characterization. The microstructure and phase composition of the multi-stage sintered composites were examined by FESEM (field emission scanning electron microscopy) and energy-dispersive spectroscopy (EDS), respectively.

Flexural specimen bars were subjected to a 3-point bend method in a universal testing instrument (Instron Model 3365, USA). The crosshead velocity was  $0.1 \text{ mm}\cdot\text{min}^{-1}$ . The

test was conducted according to ASTM C 1161-02 (ASTM, 2006) [38]. The microhardness and fractural specimen surface were polished up to a 1 $\mu$ m surface finish using diamond abrasive.

Then, the hardness and indentation fracture toughness (IFT) were determined by a microhardness machine (MMT-X7B, Hibiki Co., 2012) operated with an applied load of 500 gf and 5 kgf, respectively. Loads were applied for 15s for both cases. Minimum ten indents were generated on each specimen to estimate the average magnitude of IFT, which was determined using the following expression [39, 40]:

$$K_{IC} = 0.016 \left( \frac{E}{H_B} \right)^{1/2} \frac{L}{C^{3/2}} \quad (1)$$

In which,  $E$  denotes the elastic moduli,  $H_B$  denotes bulk hardness,  $L$  denotes the indentation load,  $a$  half diagonal length of indentation, and  $C = x+a$ , and  $x$  is the length of crack.

### 2.3 Thermal shock tests

The thermal shock resistance of the investigated composites was assessed by the indentation quenching method following the procedure established by Anderson and Rowcliffe [41]. Small samples with 10 mm  $\times$  6 mm  $\times$  3 mm were cut from the sintered specimens and polished metallographically. Four indentations were made on the surface of the polished sample by using a Vickers indenter at a load of 49.05 N in order to develop small initial cracks on the surface. The dwell time of each indentation was 15s, and a 653 $\mu$ m gap was maintained between indentations. Each indentation generated 4 cracks, and a total of 16 cracks were formed on the surface of the sample. After that, the specimens were kept inside a furnace atmosphere for 30 min at temperatures of 225 $^{\circ}$ C,

275°C, 325°C, 375°C, 425°C, 625°C, 825°C, 1025°C, and 1225°C. Afterward, the specimens were taken out from the furnace and immediately quenched in room temperature (25 °C) water. The quenched samples were characterized by XRD analysis using Cu K $\alpha$  radiation. The indentation crack length was evaluated before and after soaking using FESEM. The primary indentation crack length was restricted as the distance from the center of the indentation to the crack tip. After the thermal shock, the final crack length was equal to the initial crack length plus crack length propagated due to thermal shock.

### **3 Results and Discussion**

#### **3.1 Microstructure and mechanical properties**

The relative densities of the sintered ZMS<sub>w</sub>5 and ZMS<sub>w</sub>20 composites were 97.50% and 99.50 %, respectively. Typical XRD patterns obtained from the multistage sintered ZMS<sub>w</sub>5 and ZMS<sub>w</sub>20 composites are displayed in Fig. 2. The recorded XRD spectrums indicate that parent phases (ZrB<sub>2</sub>, MoSi<sub>2</sub>, and SiC<sub>w</sub>) and (Mo, W)Si<sub>2</sub> and WSi<sub>2</sub> phases present in all sintered samples. Furthermore, FESEM images and corresponding EDS maps of the ZMS<sub>w</sub>5 and ZMS<sub>w</sub>20 composites are illustrated in Fig. 3 and Fig. 4, respectively. Microstructural studies indicate that the MoSi<sub>2</sub> and SiC<sub>w</sub> grains are homogeneously dispersed throughout the micrograph. Micrographs illustrate that ZrB<sub>2</sub> seems gray, and MoSi<sub>2</sub> appears bright, whereas SiC whisker present in both samples looks dark. The distribution of the constituent elements in the Micrographs is confirmed by EDS mapping.

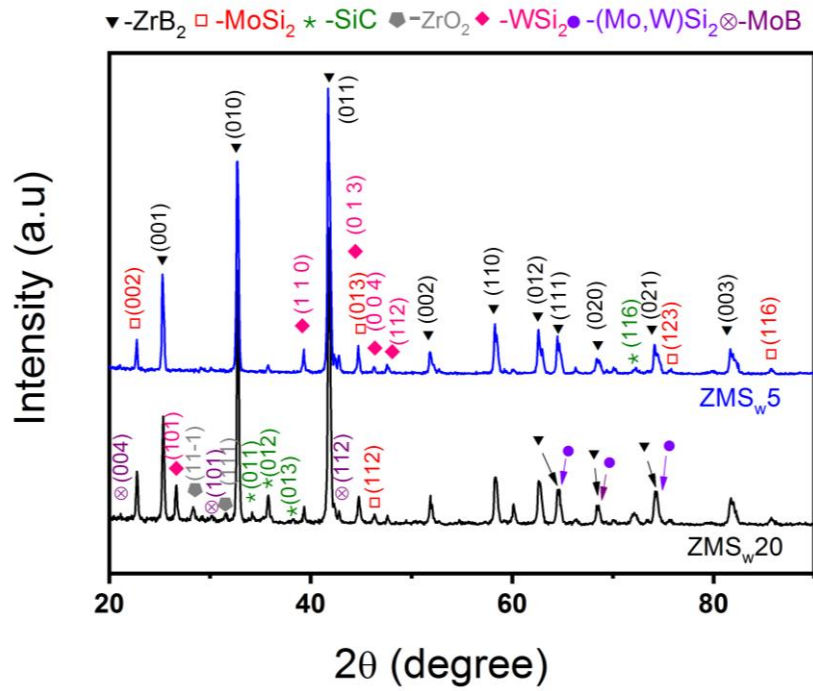


**Fig. 2.** XRD patterns of the sintered ZMS<sub>w</sub>5 and ZMS<sub>w</sub>20 composites.

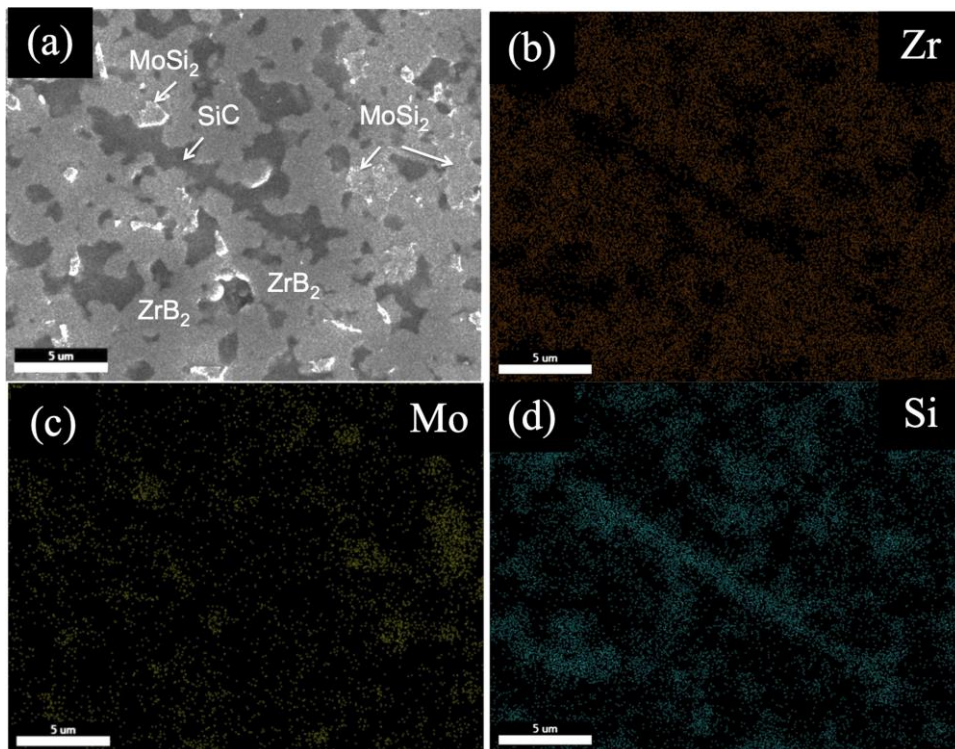


**Fig. 3.** FESEM micrograph of SPSe (a) ZMS<sub>w</sub>5 and EDS mapping of (b) Zr, (c) Mo and (d) Si

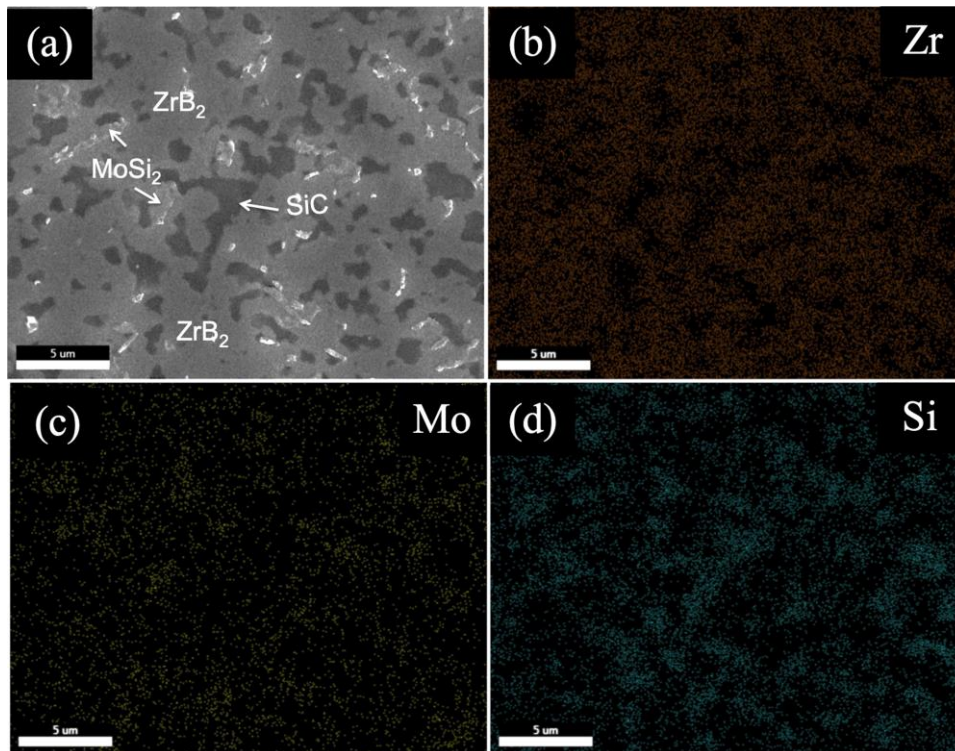


**Fig. 4 .** FESEM micrograph of SPSed (a) ZMS<sub>w</sub>20 and EDS mapping of (b) Zr, (c) Mo and (d) Si

Cracks were generated by the Vickers indentation on the surface of the sample. Figure 5 shows indentation cracks present before thermal shock in ZMS<sub>w</sub>5 composite. The mechanical and thermo-physical characteristics of the ZMS<sub>w</sub> composites are tabulated in Table 1. Especially, ZMS<sub>w</sub>20 ceramic composite provides better fracture toughness due to the presence of the elongated and huge amount of whiskers that absorb a large quantity of fracture energy. The interface between matrix and whiskers deflects cracks that cause a tortuous fracture path (Fig. 5b). In addition, the introduction of Whisker SiC can reform the fractured nature of the composite by reducing the ZrB<sub>2</sub> grain size. Therefore, fracture toughness was improved with the addition of Whisker SiC [40].

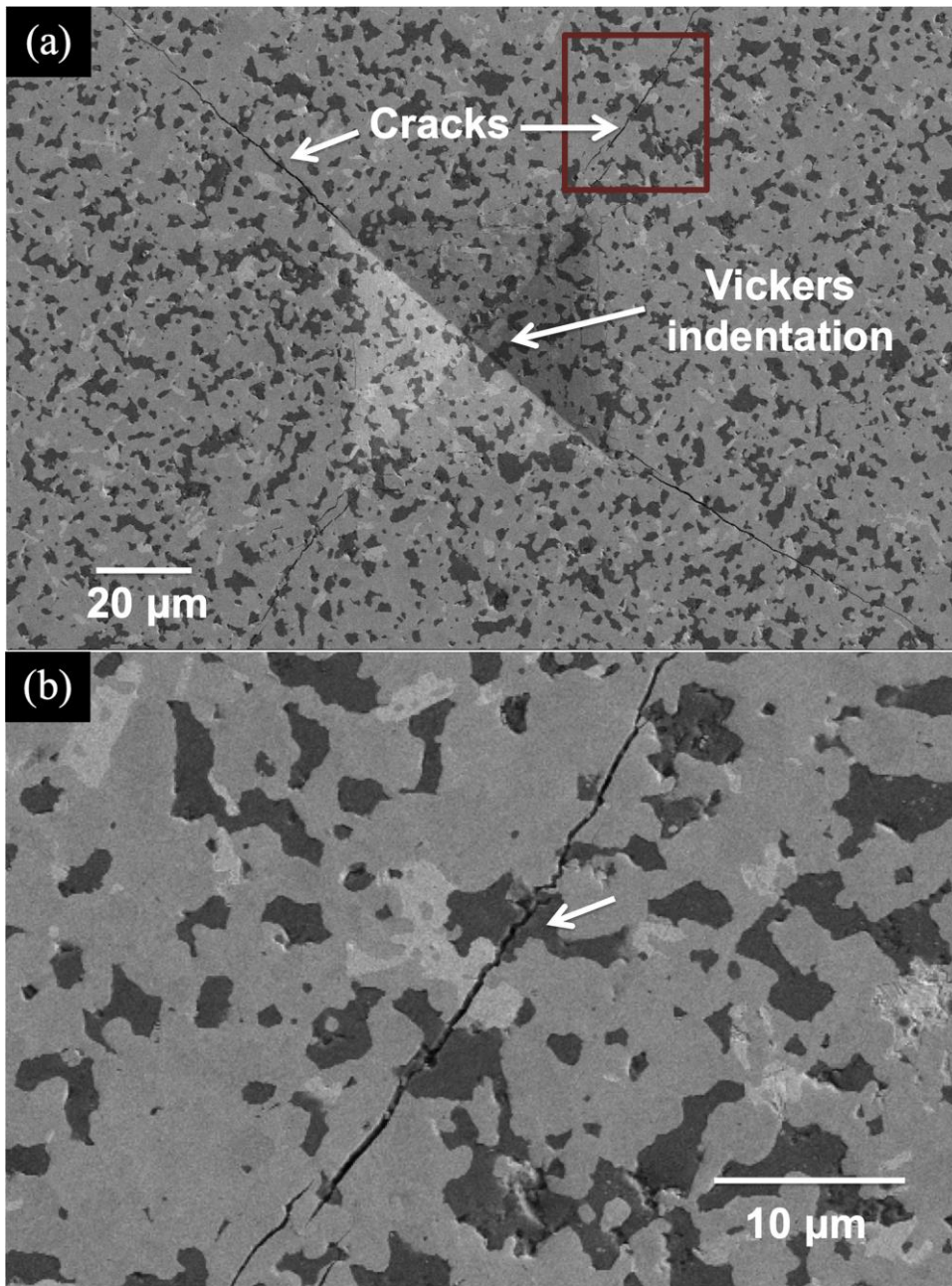


Fig. 5. Micrographs show (a) cracks are propagated from the corner of a Vickers indentation of ZMS<sub>w</sub>20 composite and (b) magnified view of the marked portion of figure (a).

**Table 1** Mechanical and thermophysical characteristics of the SPS sintered ZMS<sub>w</sub> ceramic composites

<i>Specimens</i>	<i>Poisson's ratio</i>	<i>Elastic moduli (GPa)</i>	<i>Hardness (GPa)</i>	<i>Flexural strength (MPa)</i>	<i>Fracture toughness (MPam<sup>1/2</sup>)</i>	<i>Thermal conductivity (W.m<sup>-1</sup>.K<sup>-1</sup>)</i>	<i>Thermal expansion coeff. (× 10<sup>-6</sup>) (ROM)</i>
ZMS <sub>w</sub> 5	0.15	366	14.8	414.6	5.5	65.7	6.84
ZMS <sub>w</sub> 20	0.14	414	18.2	590.8	7.4	61.5	6.38

### 3.2 Thermal shock behaviour

Thermal shock behavior is an important parameter of UHCTs in high-temperature applications. A comparative evaluation of TSR of the ZrB<sub>2</sub>-MoSi<sub>2</sub>-SiC<sub>w</sub> composites is assessed through thermal cycling, i.e., soaking at 225 °C, 275 °C, 325 °C, 375 °C, 425 °C, 625 °C, 825 °C, 1025 °C, and 1225 °C followed by water quenching. The crack length of every sample increases with an increment of temperature differential ( $\Delta T$ ). In this present investigation, the initial crack length of ZMS<sub>w</sub>5 and ZMS<sub>w</sub>20 is around 95  $\mu\text{m}$  and 76  $\mu\text{m}$ , respectively. In each sample, a total of 16 cracks are introduced after indentation. A total of two samples are examined for every pre-set temperature, so overall, 32 cracks are examined before and after every single water quenching experiment. Fig. 6. shows a schematic diagram showing cracks from at the corners and grow up after thermal shock. The original crack length is demarcated as the distance from the center of the indentation to the crack tip. After the thermal shock, the ultimate crack length equals the original crack length plus extended crack length. The system is repetitive at rising quenching temperature  $\Delta T$ , up to the critical point of  $\Delta T_c$ , at which one radial crack presented unstable growth, and the sample fails. Two parameters, i.e., a fraction of crack propagation ( $\% P$ ) and the fraction of crack extended ( $\% L$ ), were employed to study crack progression along the surface subsequently thermal shock, expressed by the following expression:

$$\%P = \frac{\Delta N}{N} \times 100\% \quad (2)$$

In which,  $N$  denotes the whole number of radial cracks generated from the indentation, and  $\Delta N$  denotes the number of total available radial cracks propagated afterward water quenching.

$$\%L = \frac{\Delta C}{C} \times 100\% \quad (3)$$

In which,  $C$  and  $\Delta C$  denote the original indentation crack length prior water quenching and the extended crack length afterward water quenching.

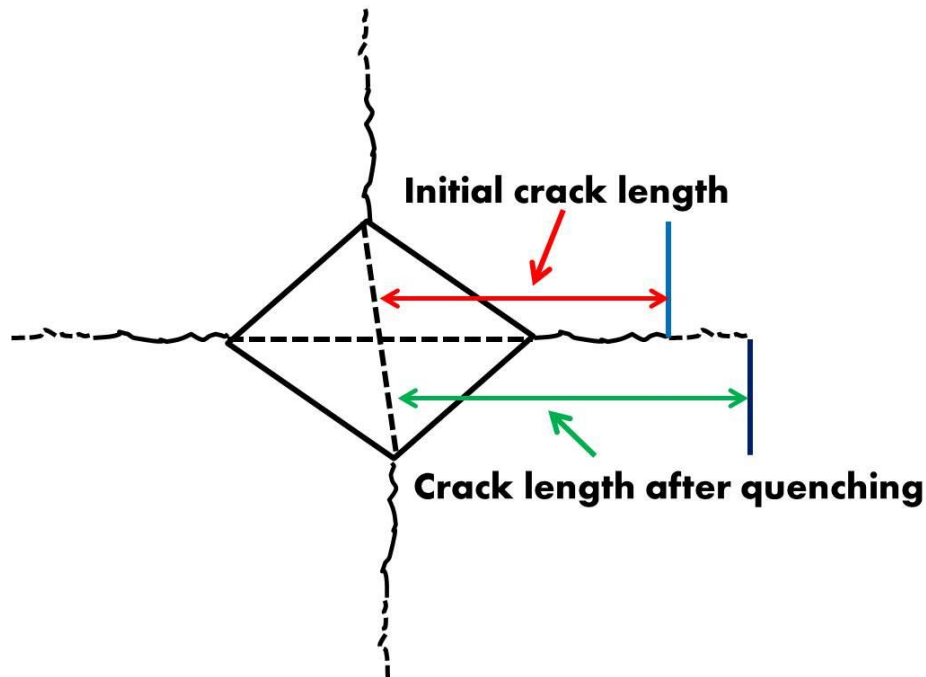


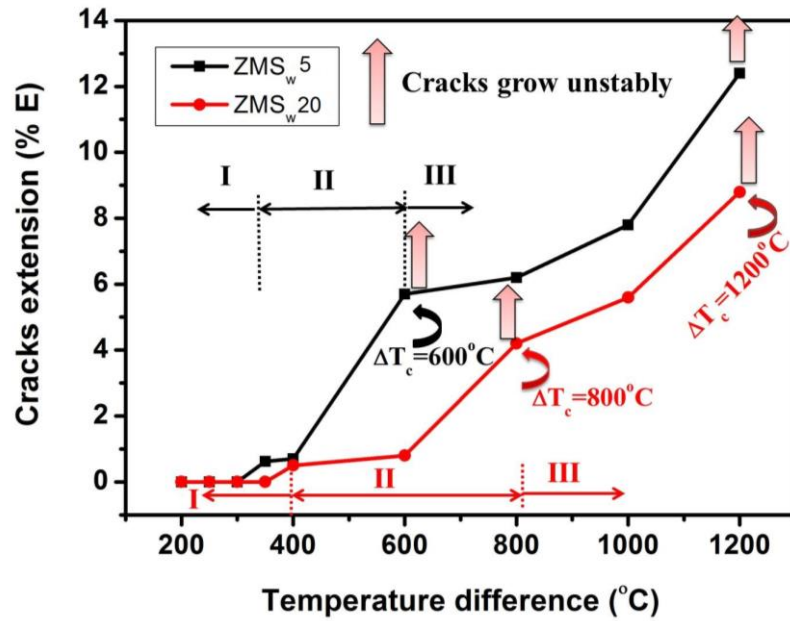
**Fig. 6.** Schematic diagram showing cracks form at the corners and grow up after quenching.

### 3.3 Indentation-quench thermal shock investigations

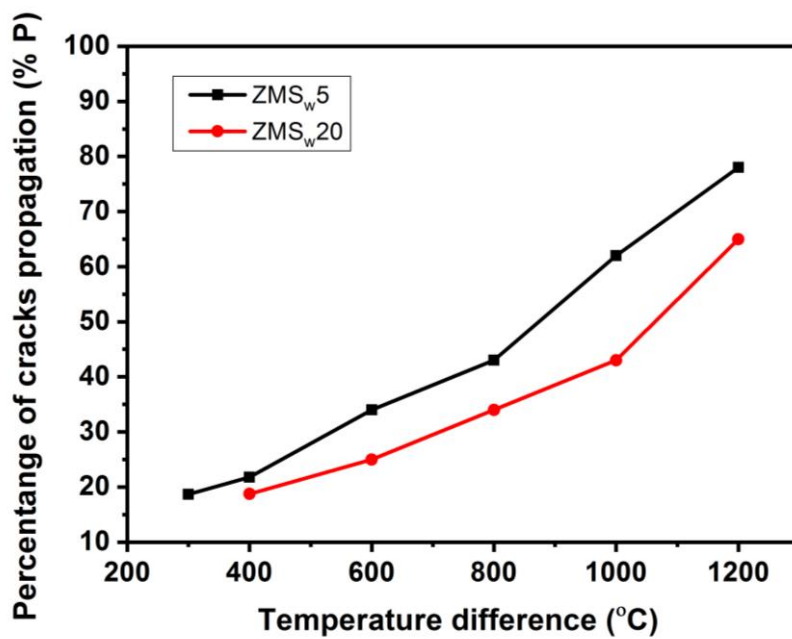
The percentages of crack extension after water quench at room temperature vs. quenching temperature differential for ZMS<sub>w</sub>5 and ZMS<sub>w</sub>20 ceramics are displayed in

Fig.7. Figure 8 shows crack propagation behavior after water quench at room temperature as a function of the quenching temperature differential for ZMS<sub>w</sub>5 and ZMS<sub>w</sub>20 composites sintered via multi-stage sintering route. It is observed that the fractions of crack extension and crack propagation are significantly related to temperature difference ( $\Delta T$ ). The higher thermal-shock temperature difference shows a higher percentage of crack extension and cracks propagation. The ZMS<sub>w</sub>5 ceramics shows weak crack-growth resistance behavior after quenching. Moreover, %E and %P are greater than for the ZMS<sub>w</sub>20 ceramics. Figures 7 and 8 show that the ZMS<sub>w</sub>5 and ZMS<sub>w</sub>20 ceramic composites have an identical outline of crack progression. Hence, the crack progression can be parted into three sections. There is no significant crack growth at low  $\Delta T$  (Section I). Cracks grow stably at medium  $\Delta T$  (Section II). Cracks grow unstably over a certain high  $\Delta T$  (Section III). The critical  $\Delta T_c$  for unstable crack growth of the ZMS<sub>w</sub>-20 ceramic is 800 °C, which is higher than that of the ZMS<sub>w</sub>5 composite ( $\Delta T_c$  value for the ZMS<sub>w</sub>5 is 600 °C). This is confirmed that multi-stage sintered ZMS<sub>w</sub>20 ceramics express superior thermal shock resistance behavior than multi-stage sintered ZMS<sub>w</sub>5 ceramic. Thermal shock resistance strongly depends on thermal and mechanical characteristics such as thermal conductivity, fracture toughness, elastic modulus, strength, and thermal expansion coefficient. Besides, all these properties are fundamentally related to the microstructure, density, chemical composition, and fabrication procedure of composites. Both ZMS<sub>w</sub>5 and ZMS<sub>w</sub>20 ceramics were prepared by spark plasma sintering via multi-stage sintering route. Even both ceramics have a similar chemical composition and almost the same microstructure. Consequently, one important question is why ZMS<sub>w</sub>20 has better thermal shock resistance than ZMS<sub>w</sub>5. Ultra-high temperature ceramics (UHTCs) are candidates for applications under extreme environments such as thermal shielding elements and sharp leading edges for

hypersonic re-entry vehicles, advanced nuclear fuels, rocket engines, nuclear reactors, furnaces elements, plasma -arc- electrodes, and refractory crucibles. So, understanding the temperature distribution and corresponding thermal stresses in UHTC materials under high temperatures is essential in order to assess their integrity. The TSR of ceramics is found to be very sensorial to their temperature-related material properties. For ZMS<sub>w</sub>20,  $\Delta T_c$  for unstable crack propagation is 800 °C, superior to the ZMS<sub>w</sub>5. It could be investigated from Fig. 8, the crack progressions in both inspected samples introduced a stepwise model, which is directed that the temperature for crack extension is not steady because of the existence of various stresses at the crack tip. During multi-stage sintering, the formation of (Mo, W)Si<sub>2</sub> is a product of the sintering reaction. In this viewpoint, the secondary phase of (Mo, W)Si<sub>2</sub>, which has a more significant CTE ( $8.3-6.7 \times 10^{-6}/K$ ) [42] than the matrix of ZrB<sub>2</sub> ( $6.91 \times 10^{-6} K^{-1}$ )[43], results in the development of compressive residual stress during cooling from the sintering temperature. Such high compressive residual stress resists crack extension during thermal shock. Therefore, cracks in the ZMS<sub>w</sub>5 composite have grown unstably at  $\Delta T \sim 600$  °C, whereas cracks in the ZMS<sub>w</sub>20 composite have grown unstably until  $\Delta T > 800$  °C.



**Fig. 7.** The percentage of crack extension after water quench at room temperature vs. quenching temperature differential for ZMS<sub>w</sub>5 and ZMS<sub>w</sub>20 composites.



**Fig. 8.** The percentage of crack propagation (% P) after water quench at room temperature vs. quenching temperature differential for ZMS<sub>w</sub>5 and ZMS<sub>w</sub>20 composites.

### 3.4 Oxide Phase identification upon thermal shock test

Typical XRD spectrums of the quenched surface of ZMS<sub>w</sub>5 and ZMS<sub>w</sub>20 composites are displayed in Fig. 9. Figure 9 reveals that the surface phases of ZMS<sub>w</sub>5 and ZMS<sub>w</sub>20 composites after water quenched at a series of temperature differences are consistent with primary materials. The XRD results also specify that the manifestation of oxides of ZrO<sub>2</sub> and other oxide phases of Mo<sub>5</sub>Si<sub>3</sub> and ZrSiO<sub>4</sub>. ZrB<sub>2</sub> is partly oxidized to ZrO<sub>2</sub>. The relatively more peaks of the ZrO<sub>2</sub> phases are detected in ZMS<sub>w</sub>5 (Fig. 9(a)). The transformation of ZrB<sub>2</sub> to ZrO<sub>2</sub> can be progressed by raising the temperature differences. The amount of ZrO<sub>2</sub> expresses an increasing trend from  $\Delta T=800$  °C. However, poor oxidation resistance of ZMS<sub>w</sub>5 at 1200 °C exhibits the presence of more amount of ZrO<sub>2</sub> phases. Overall, thermal shock for  $\Delta T = 600$  °C is less damaging than that for  $\Delta T = 800$  °C due to the presence of a high amount of oxide phase. However, this oxide phase is not favorable to resist crack growth during thermal shock.

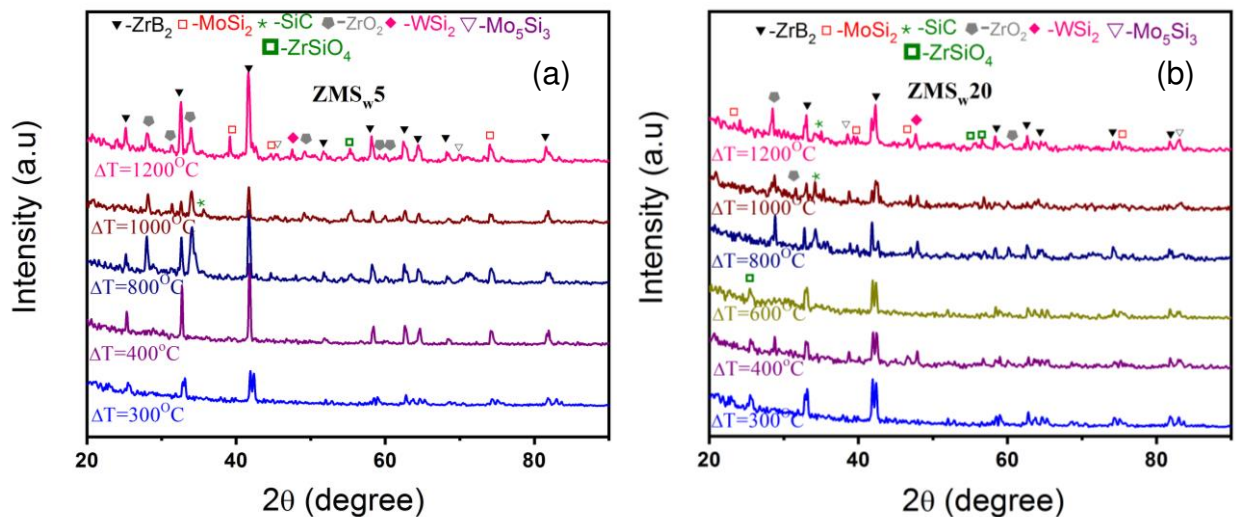


**Fig. 9.** XRD spectrums of sample surface afterward thermal shock at different temperature differences: (a) ZMS<sub>w</sub>5 and (b) ZMS<sub>w</sub>20.

### 3.5 Theoretical study of indentation thermal shock behaviour

The indentation of thermal shock mechanism should be analyzed by measuring stress intensity, which is generated at the indentation crack tips. For the ZMS<sub>w</sub> ceramic composites, the total stress intensity factor at the indentation crack tip is exposed after water quenching ( $K_I$ ) = residual stress intensity ( $K_r$ ) is prompted by indentation load + thermal stress intensity by thermal shock experiment ( $K_{th}$ )

$$K_I = K_r + K_{th} \quad (4)$$

$K_r$  can be defined by:

$$K_r = \aleph_r P_v \quad (5)$$

Where,  $\aleph_r$  is a constant value which is estimated as  $0.016 (E/H)^{0.5}$ ,  $P_v$  and  $c$  represent the Vickers indentation load and Vickers indentation flaw of length, respectively.

$E$  denotes the elastic moduli;  $H$  denotes hardness of the specimens.

In the case of thermal shock, the thermal stress intensity ( $K_{th}$ ) of the indentation crack method is only measured at the surface of the specimen and is expressed by:

$$K_{th} = \sigma_{th} (\pi \varphi c)^{1/2} \quad (6)$$

Where,  $\varphi$  represents a geometry constant factor for a crack of semi-elliptical surface ( $\varphi = 4/\pi^2$ ), which is more or less the shape of median-radial indentation cracks.

The thermal stress is described as follows:

$$\sigma_{th} = f(\beta) \frac{E\alpha}{1-\nu} \Delta T \quad (7)$$

Where,  $\alpha$  is the coefficient of thermal expansion,  $\Delta T$  denotes the temperature difference and  $\nu$  denotes the Poisson's ratio of the specimen.

$f(\beta)$  is a geometry factor and it is a function of heat transfer condition as well as the Biot modulus of  $\beta$  and it is represented by:

$$f(\beta) = \left[ M + \frac{N}{\beta} + Z \cdot \exp\left(-\frac{W}{\beta}\right) \right]^{-1} \quad (8)$$

$$\beta = \frac{hd}{k} \quad (9)$$

Where,  $d$  denotes the characteristic length of heat transfer (i.e., the thickness of the specimen/2),  $h$  represents the coefficient of heat transfer between specimens and the water cooling medium, and  $k$  represents the thermal conductivity of the specimen. In the case of cylindrical indentation specimens, the constant values of  $M$ ,  $N$ ,  $Z$ , and  $W$  are 3.15, 1.33, -0.266, and 5.14, respectively. [44].

Hence, after combining all equations, the total stress intensity ( $K_I$ ) of an indentation crack for ZMS<sub>w</sub> composite can be defined as follows [45]:

$$K_I = \kappa_r P c^{-1.5} + f(\beta) \frac{E\alpha}{1-\nu} \Delta T (\pi\phi c)^{1/2} \quad (10)$$

The assumptions of mechanical equilibrium are considered for this equation (equation 10).  $K_I$  will be determined to find out whether the indentation crack will propagate or not, even it also finds that the indentation crack propagates either a stable or unstable form. The indentation crack will expand in unstable form during thermal shock loading if

$$K_I \geq K_{IC} \quad (11)$$

and

$$\frac{dK_I}{dc} \leq \frac{dK_{IC}}{dc} \quad (12)$$

Where,  $K_{IC}$  is the indentation fracture toughness of the specimen.

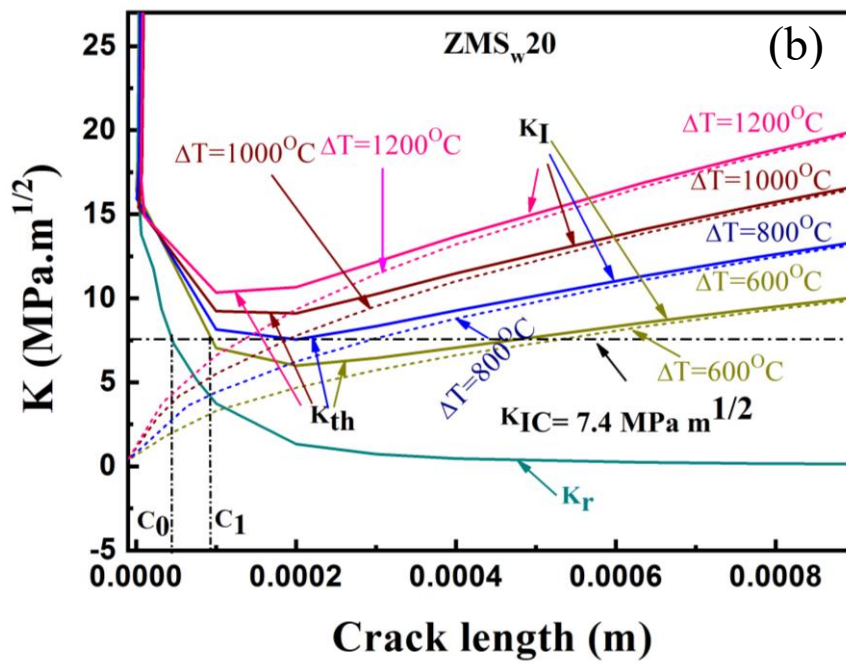
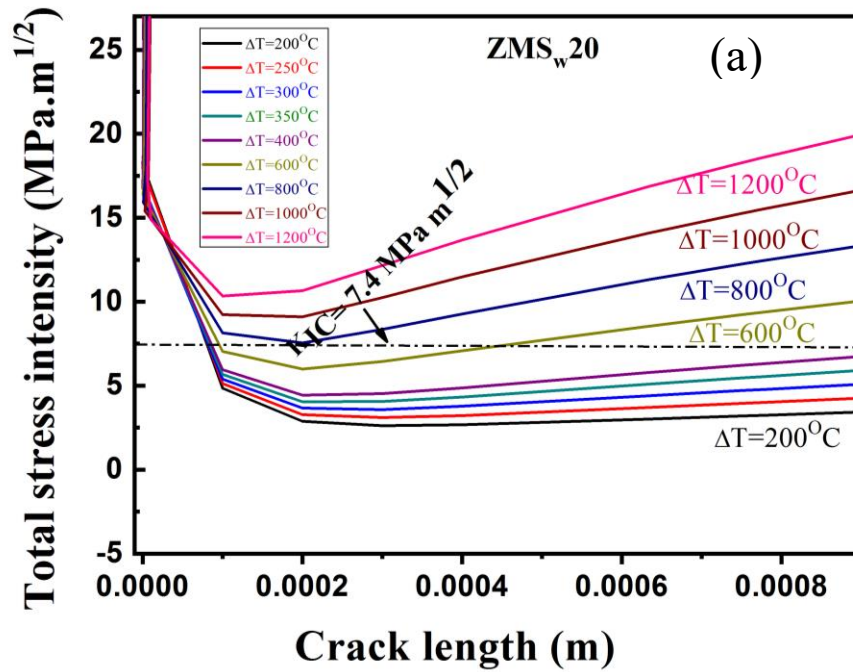


**Fig. 10.** Total stress intensity with various  $\Delta T$  vs. of crack length and stress intensity with certain  $\Delta T$  of Vickers indentation cracks at the surface vs. indentation crack length after water quenching for  $ZMS_w20$  ceramics (a,b).

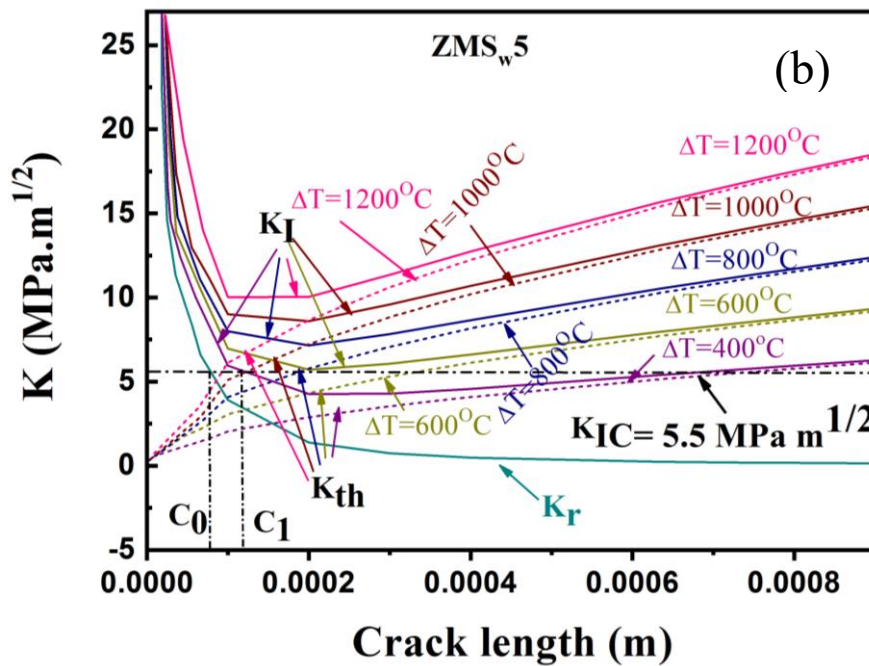
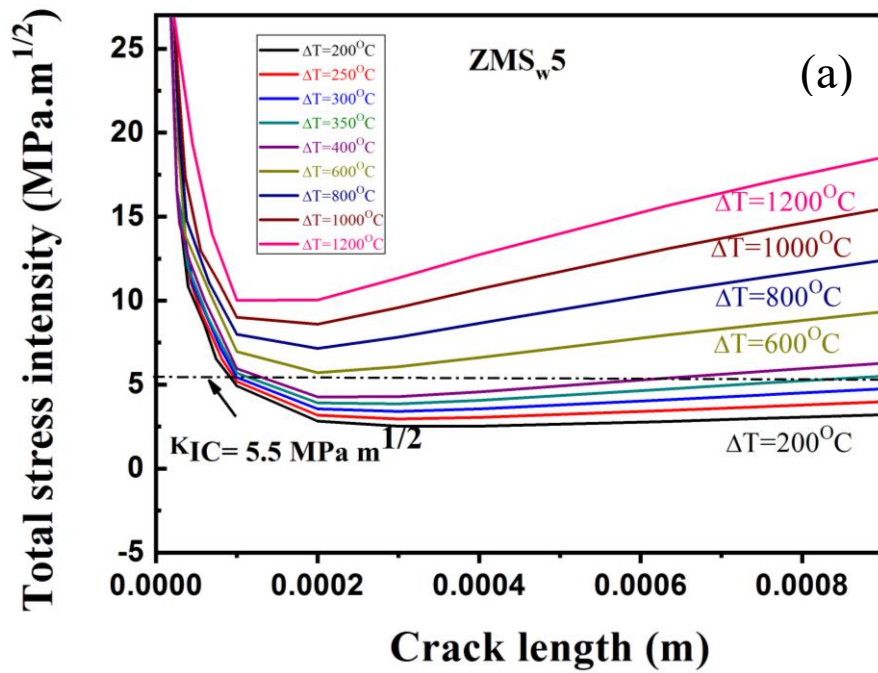


**Fig. 11.** (a) Total stress intensity with various  $\Delta T$  vs. crack length and (b) stress intensity with certain  $\Delta T$  of Vickers indentation cracks at the surface vs. indentation crack length after water quenching for  $ZMS_w5$  ceramics.

The total stress intensity ( $K_I$ ) at the indentation crack tip vs. crack length ( $c$ ) for the ZMS<sub>w</sub>20 composite is shown in Fig.10 (a), which are quenched under several thermal shock temperatures. The value of  $K_I$  can be measured according to Eq.(10). The value of  $K_I$  rises with increasing  $\Delta T$  (Figure 10 (a)). Every  $K_I$  has a minimum value at all  $\Delta T$ . Each minimum value of  $K_I$  rises with the rise in temperature difference  $\Delta T$ . When  $\Delta T > 800$  °C, the indentation cracks grow unstably because the  $K_I$  value higher than the fracture toughness ( $K_{IC}$ ). Fig.10 (b) demonstrates the variation between stress intensity and indentation crack length for ZMS<sub>w</sub>20 ceramic when the samples are water quenched with the various temperature of 600 °C, 800 °C, 1000 °C, and 1200 °C. The  $K_{th}$  and  $K_r$  at various temperature differences are calculated through Eq.(6) and Eq.(5), respectively. Figure 10 (b) shows that  $K_r$  decreases while  $K_{th}$  and  $K_I$  increase with increasing crack length. While  $\Delta T=600$  °C, the crack length is small ( $C=C_0$ ,  $C_0$  means indentation crack lengths in the stress-out surfaces), and  $K_r$  is higher than the thermal stress intensity ( $K_{th}$ ) as the crack length increases. For those reasons, the  $K_I$  reduces as the crack length raising. When  $K_I$  reduces or equal to  $K_{IC}$ , the crack growth is prevented at  $C=C_1$  ( $C_1$  denotes indentation crack lengths in the residually stressed surfaces). Thermal shock temperature variance  $\Delta T$  is prolonged, which confirms that cracks can propagate continuously. While  $\Delta T \geq 800$  °C,  $K_I$  will be continuously increased than  $K_{IC}$  in every period. Hence, indentation cracks will propagate in unstable while  $\Delta T \geq 800$  °C. The critical thermal shock temperature difference is calculated from the theoretical analysis at 800 °C, which is also the best agreement with the experimentally obtained outcomes. Figure 11 shows that ZMS<sub>w</sub>5 also follows the same patterns as ZMS<sub>w</sub>20. For ZMS<sub>w</sub>5, the cracks will propagate unstably when  $\Delta T \geq 600$  °C. It also shows the best agreement with the experimentally obtained outcomes. Finally, it can be noted that ZMS<sub>w</sub>20 ceramics shows better thermal shock resistance than ZMS<sub>w</sub>5 ceramics because

of the presence of high residual stress in ZMS<sub>w</sub>20 than ZMS<sub>w</sub>5 samples. Thus, crack propagation in the ZMS<sub>w</sub>20 composite needs an upper thermal shock temperature than that for the ZMS<sub>w</sub>5 composite. For this reason, the critical thermal shock temperature ( $\Delta T_c$ ) of 800 °C in ZMS<sub>w</sub>20 is higher than 600 °C in ZMS<sub>w</sub>5.

### 3.6 Microhardness

The changes in microhardness of both the ZMS<sub>w</sub> ceramics due to thermal shock are displayed in Fig. 12. It is explicit from Fig. 12 that (i) hardness of both ceramic losses with a rising thermal shock temperature ( $\Delta T$ ); (ii) net drop in hardness detected for the ZMS<sub>w</sub>20 ceramic is lesser than that ZMS<sub>w</sub>5 composite. Figure 9 reveals that the generation of an intermittent scale of ZrO<sub>2</sub> is more for the ZMS<sub>w</sub>5 composite. The CTE of ZrO<sub>2</sub> ( $10.3 \times 10^{-6} \text{ K}^{-1}$ ) [5] is considerably greater than that of matrix ZrB<sub>2</sub>, while its thermal conductivity is also lower (2.0 W/mK). This ZrO<sub>2</sub> scale contributed to thermal stress due to the huge dissimilarity of thermal properties of the composites leads to spallation of the surface scale. Moreover, the mismatch of CTE of the W-rich interfacial phase and matrix phase or oxidation of W succeeded by evaporation of WO<sub>3</sub> can play an essential function in damage through thermal shock, mainly on soaking at temperatures  $\Delta T \geq 1000 \text{ }^\circ\text{C}$ .

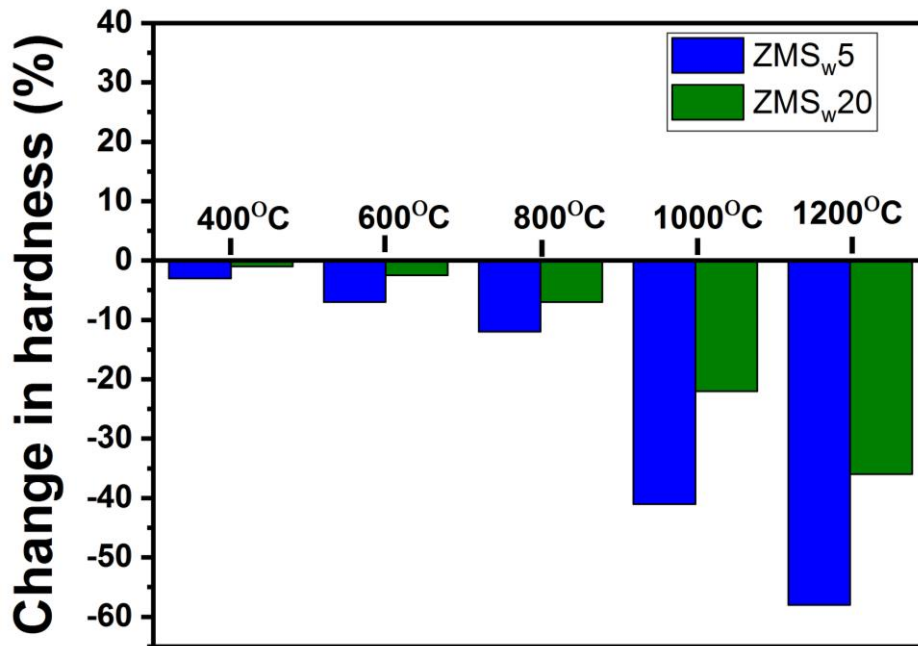


**Fig. 12.** Bar chart displaying changes in hardness of the ZMS<sub>w</sub> composites due to thermal shock through at soaking various temperatures.

#### 4 Conclusions

The TSR of ZMS<sub>w</sub>5 and ZMS<sub>w</sub>20 composites are investigated through the indentation-quench approach. The critical thermal shock temperatures of ZMS<sub>w</sub>5 and ZMS<sub>w</sub>20 are 600°C and 800°C, respectively, which indicate that the ZMS<sub>w</sub>20 composite exhibits better TSR under quenching conditions, compared to that of ZMS<sub>w</sub>5 composites. The theoretical analysis confirms that the results have a good agreement with the experimentally obtained outcomes. High residual stress is observed in multi-stage SPS sintered ZMS<sub>w</sub>20 composite. Such high compressive residual stress is a barrier or obstacle to the stress field intensity at the crack tip. It contributes to the improvement in crack progression resistance during thermal shock. However, poor oxidation resistance of ZMS<sub>w</sub>5 at 1200 °C exhibits more ZrO<sub>2</sub> phases. This oxide phase is not favorable to resist crack growth during thermal shock. For this reason, an increment of SiC<sub>w</sub> content

reduces the crack growth, and that successively enhances the thermal shock of the composites. The drop in hardness due to thermal shock for the ZMS<sub>w</sub>20 composite is less than that of the ZMS<sub>w</sub>5 composite.

### **Acknowledgment**

The authors express their sincere gratitude to Professor Rahul Mitra, and Professor Tapas Laha IIT Kharagpur, for providing the sintering facility. The authors also thank Mr. Sandip Ruidas, Technical personnel at Centre of Excellence in Advanced Materials NIT Durgapur, for FESEM analysis.

## Reference

- [1] Golla BR, Mukhopadhyay A, Basu B, Thimmapp SK. Review on ultra-high temperature boride ceramics. *Prog Mater Sci* 2020, **111**:100651.
- [2] Natali M, Kenny JM, Torre L. Science and technology of polymeric ablative materials for thermal protection systems and propulsion devices: A review. *Prog Mater Sci* 2016, **84**:192-275.
- [3] Han Q, Sun C, Tao Y, Li Z, Zhang Y, Che Y. Thermal protection of a hypersonic vehicle by modulating stagnation-point heat flux. *Aerosp Sci Technol* 2020, **98**:105673.
- [4] Kolodziej P. *Aerothermal performance constraints for hypervelocity small radius unswept leading edges and nose tips*. NASA Technical Memorandum, California 1997, 1122047.
- [5] Mallik M, Kailath AJ, Ray KK, Mitra R. Effect of SiC content on electrical, thermal and ablative properties of pressureless sintered ZrB<sub>2</sub>-based ultrahigh temperature ceramic composites. *J Eur Ceram Soc* 2017, **37**:559–572.
- [6] Xue L, Su ZA, Yang X, Huang D, Yin T, Liu C, Huang Q. Microstructure and ablation behavior of C/C–HfC composites prepared by precursor infiltration and pyrolysis. *Corros Sci* 2015, **94**:165–170.
- [7] Zoli L, Vinci A, Galizia P, Melandri C, Sciti D. On the thermal shock resistance and mechanical properties of novel unidirectional UHTCMCs for extreme environments. *Sci Rep* 2018, **8**:9148.
- [8] Fahrenholtz WG, Hilmas GE, Talmy IG, Zaykoski JA. Refractory diborides of zirconium and hafnium. *J Am Ceram Soc* 2007, **90**:1347–1364.
- [9] Asla MS, Nayebib B, Ahmadi Z, Zamharirc MJ, Shokouhimehr M. Effects of carbon additives on the properties of ZrB<sub>2</sub>-based composites: A review. *Ceram Int* 2018, **44**:7334-7348.
- [10] Upadhya K, Yang JM, Hoffmann WP. Materials for ultrahigh temperature structural applications. *Am Ceram Soc Bull* 1997, **76**:51–56.
- [11] Gasch MJ, Ellerby DT, Johnson SM. Ultra-high temperature ceramic composites. *Handbook of Ceramic Composites*. Bansal NP, Edi: Boston: Kluwer Academic Publishers, 2005: 197–224.
- [12] Samsonov GV, Vinitiskii IM. *Handbook of Refractory Compounds*. New York: IFI/PLENUM; 1980.

- [13] Cutler RA. Engineering properties of borides. *Ceramics and Glasses, Engineered Materials Handbook*. Schneider SJ, Edi: ASM International, Materials Park, OH: 1992, 4:787–803.
- [14] Sciti D, Guicciardi S, Bellosi A, Pezzotti G. Properties of a pressureless-sintered ZrB<sub>2</sub>–MoSi<sub>2</sub> ceramic composites. *J Am Ceram Soc* 2006, **89**:2320–2322.
- [15] Jackson TA, Eklund DR, Fink AJ. High speed propulsion: Performance advantage of advanced materials. *J Mater Sci* 2004, **39**: 5905-5913.
- [16] Wie DMV, Drewry DG, King DE, Hudson CM. The hypersonic environment: Required operating conditions and design challenges. *J Mater Sci* 2004, **39**: 5915-5924.
- [17] Sonber JK, Suri AK. Synthesis and consolidation of zirconium diboride: review. *Adv Appl ceram* 2011, **110**:321-334.
- [18] Mashhadia M, Shambulia M, Safi S. Effect of MoSi<sub>2</sub> addition and particle size of SiC on pressureless sintering behavior and mechanical properties of ZrB<sub>2</sub>–SiC–MoSi<sub>2</sub> composites. *J Mater Res Technol* 2016, **5**:200–205.
- [19] Mallik M, Ray KK, Mitra R. Effect of Si<sub>3</sub>N<sub>4</sub> addition on oxidation resistance of ZrB<sub>2</sub>-SiC composites. *Coatings* 2017, **7**:92.
- [20] Mallik M, Ray KK, Mitra R. Effect of Si<sub>3</sub>N<sub>4</sub> addition on compressive creep behaviour of hot pressed ZrB<sub>2</sub>-SiC composites. *J Am Ceram Soc* 2014, **97**: 2957–2964.
- [21] Sciti D, Brach M, Bellosi A. Long-term oxidation behavior and mechanical strength degradation of a pressurelessly sintered ZrB<sub>2</sub>–MoSi<sub>2</sub> ceramic. *Scr Mater* 2005, **53**: 1297–1302.
- [22] Balak Z, Zakeri M, Rahimipour M, Salahi E. Taguchi design and hardness optimization of ZrB<sub>2</sub>-based composites reinforced with chopped carbon fiber and different additives and prepared By SPS. *J Alloys Compd* 2015, **639**:617–625.
- [23] He R, Tong Z, Zhang K, Fang D. Mechanical and electrical properties of MoSi<sub>2</sub>-based ceramics with various ZrB<sub>2</sub>-20 vol% SiC as additives for ultra high temperature heating element. *Ceram Int* 2018, **44**:1041–1045.
- [24] Gupta N, Mukhopadhyay A, Pavani K, Basu B. Spark plasma sintering of novel ZrB<sub>2</sub>-SiC-TiSi<sub>2</sub> composites with better mechanical properties. *Mater Sci Eng A* 2012, **534**:111–118.
- [25] Opila E, Levine S, Lorincz J. Oxidation of ZrB<sub>2</sub>-and HfB<sub>2</sub>-based ultra-high temperature ceramics: effect of Ta additions. *J Mater Sci* 2004, **39**: 5969–5977.

- [26] Mallik M, Pan S, Roy H. Fracture toughness measurement of hot pressed ZrB<sub>2</sub>-MoSi<sub>2</sub> composite. *Int J Curr Eng Technol* 2013, **3**:1647–1652.
- [27] Mallik M, Mitra P, Srivastava N, Narain A, Dastidar SG, Singh A, Paul TR. Abrasive wear performance of zirconium diboride based ceramic composite. *Int J Refract Metals Hard Mater* 2019, **79**:224–232.
- [28] Paul TR, Mondal MK, Mallik M. Dry sliding wear response of ZrB<sub>2</sub>-20vol.% MoSi<sub>2</sub> composite. *Mater Today Proc* 2018, **5**:7174–7183.
- [29] Monteverde F. The addition of SiC particles into a MoSi<sub>2</sub>-doped ZrB<sub>2</sub> matrix: Effects on densification, microstructure and thermo-physical properties. *Mater Chem Phys* 2009, **113**:626–633.
- [30] Silvestroni L, Stricker K, Sciti D, Kleebe HJ. Understanding the oxidation behavior of a ZrB<sub>2</sub>-MoSi<sub>2</sub> composite at ultra-high temperatures. *Acta Mater* 2018, **151**:216-228.
- [31] Guo S, Nishimura T, Mizuguchi T, Kagawa Y. Mechanical properties of hot-pressed ZrB<sub>2</sub>-MoSi<sub>2</sub>-SiC composites. *J Eur Ceram Soc* 2008, **28**: 1891-1898.
- [32] Wang Y, Zhu M, Cheng L, Zhang L. Fabrication of SiC<sub>w</sub> reinforced ZrB<sub>2</sub>-based ceramics. *Ceram Int* 2010, **36**:1787–1790.
- [33] Zhang X, Xu L, Du S, Han J, Hu P, Han W. Fabrication and mechanical properties of ZrB<sub>2</sub>-SiC<sub>w</sub> ceramic matrix composite. *Mater Lett* 2008, **62**: 1058–1060.
- [34] Zhnag P, Hu P, Zhnag X, Han J, Meng S. Processing and characterization of ZrB<sub>2</sub>-SiC<sub>w</sub> ultra-high temperature ceramics. *J Alloys Compd* 2009, **472**:358–362.
- [35] Li CW, Lin YM, Wang MF, Wang CA. Preparation and mechanical properties of ZrB<sub>2</sub>-based ceramics using MoSi<sub>2</sub> as sintering aids. *Front Mater Sci China* 2010, **4**: 271-275.
- [36] Paul TR, Mondal MK, Mallik M. Abrasive wear performance and wear map of ZrB<sub>2</sub>-MoSi<sub>2</sub>-SiC<sub>w</sub> composites. *J Eur Ceram Soc* 2021, **41**:3227–3251.
- [37] Desai AM, Paul TR, Mallik M. Processing and wear characterization of fly ash particle reinforced Al matrix composites. *Mater Res Express* 2020, **7(1)**:1-14.
- [38] ASTM C1161-02 Standard Test Method for Flexural Strength of Advanced Ceramics at Ambient Temperature.
- [39] Anstis GR, Chantikul P, Lawn BR, Marshall DB. A critical evaluation of indentation techniques for measuring fracture toughness: I, direct crack measurements. *J Am Ceram Soc* 1981; **64**:533–538.

- [40] Paul TR, Mondal MK, Mallik M. Microstructure dependent physical and mechanical properties of spark plasma sintered  $ZrB_2$ - $MoSi_2$ - $SiC_w$  composites. *Int J Refract Metals Hard Mater* 2019, **79**:131–137.
- [41] Andersson T, Rowcliffe DJ. Indentation Thermal shock Test for ceramics. *J Am Ceram Soc* 1996, **79**:1509–1514.
- [42] Zhang H, Lv J, Zhuang S, Chen Y, Gu S. Effect of  $WSi_2$  and  $Si_3N_4$  contents on the thermal expansion behaviors of  $(Mo,W)Si_2$ - $Si_3N_4$  composites. *Ceram Int* 2017, **43**:2847–2852.
- [43] Zhu S, Fahrenholtz WG, Hilmas GE, Zhang SC. Pressureless sintering of zirconium diboride using boron carbide and carbon additions. *J Am Ceram Soc* 2007, **90**:3660–3663.
- [44] Collin M, Rowcliffe D. Analysis and prediction of thermal Shock in brittle materials. *Acta Mater* 2000, **48**:1655–1665.
- [45] Tancret F, Osterstock F. The Vickers indentation technique used to evaluate thermal shock resistance of brittle materials. *Scr Mater* 1997, **37(4)**: 443–447.

# Figures

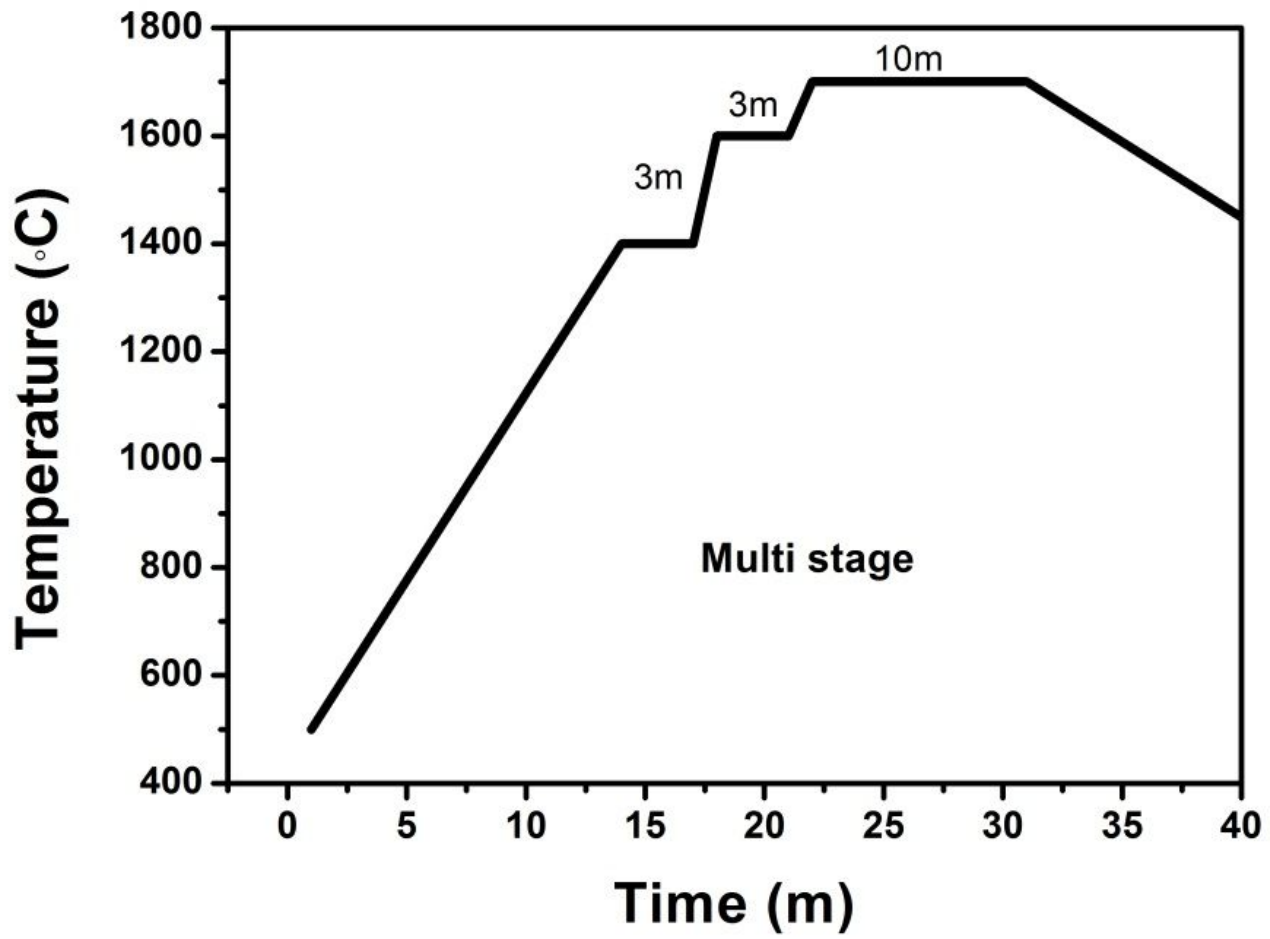


Figure 1

Graphical representation of the multistage SPS sintering heating cycle.

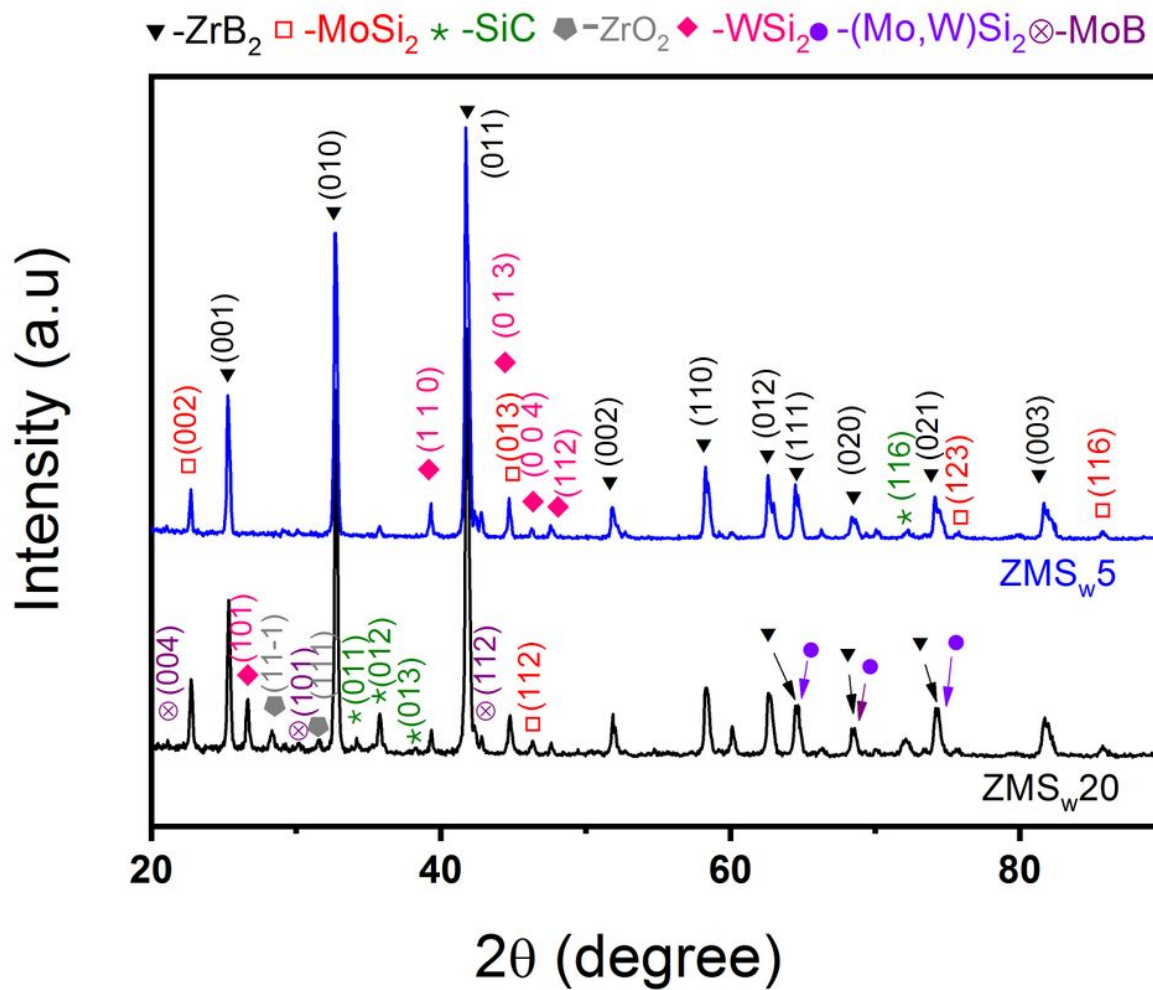


Figure 2

XRD patterns of the sintered ZMSw5 and ZMSw20 composites.

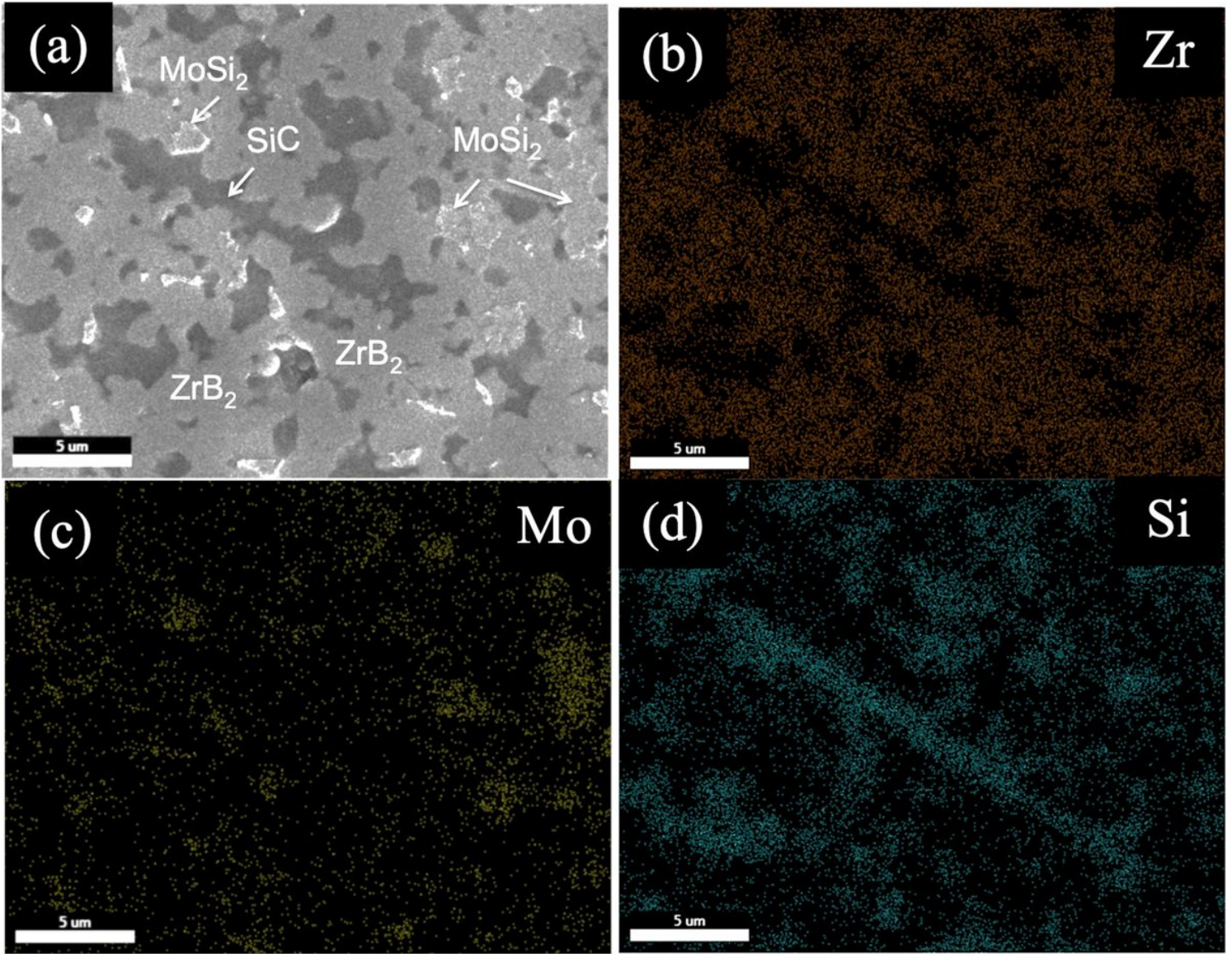


Figure 3

FESEM micrograph of SPSed (a) ZMSw5 and EDS mapping of (b) Zr, (c) Mo and (d) Si

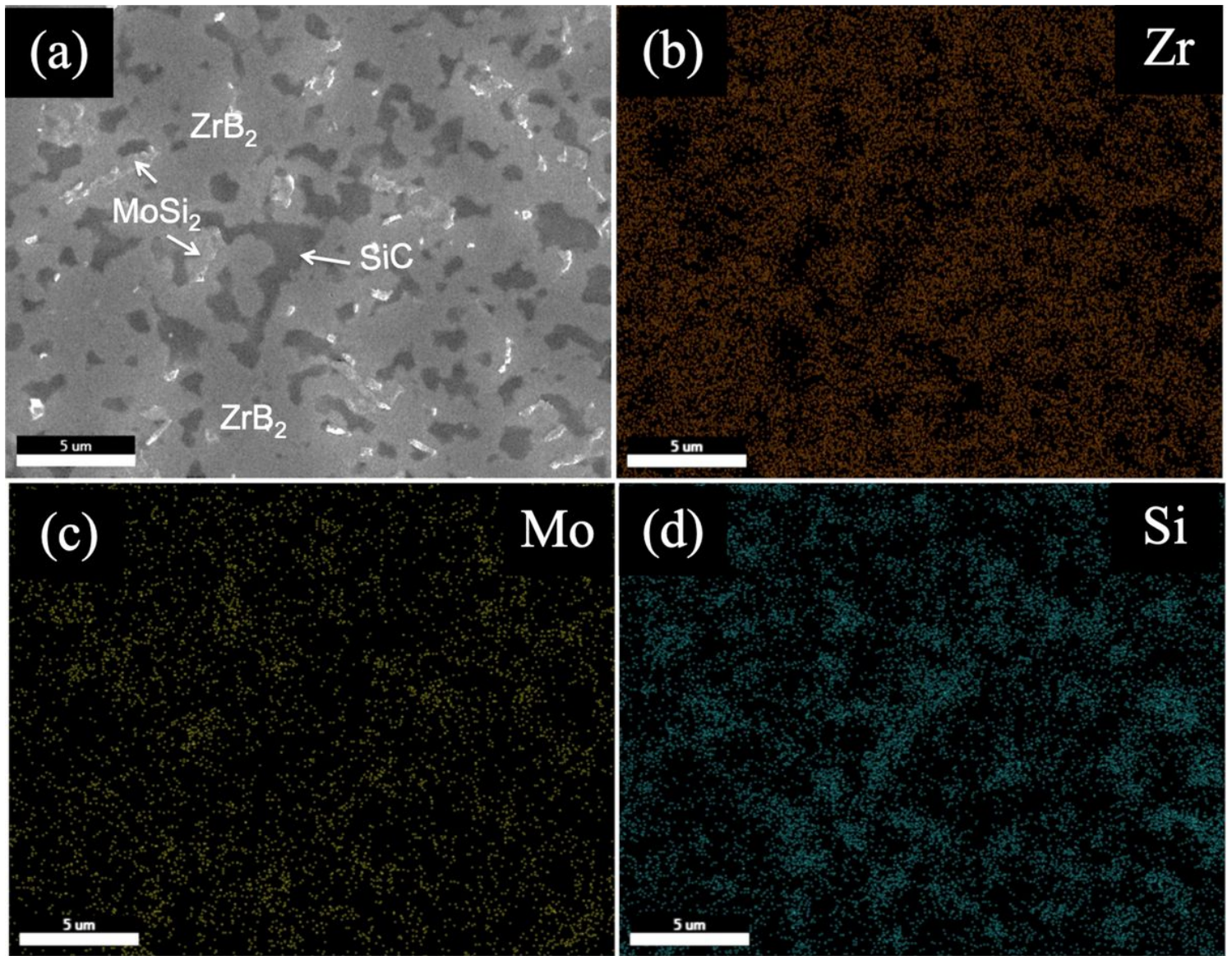
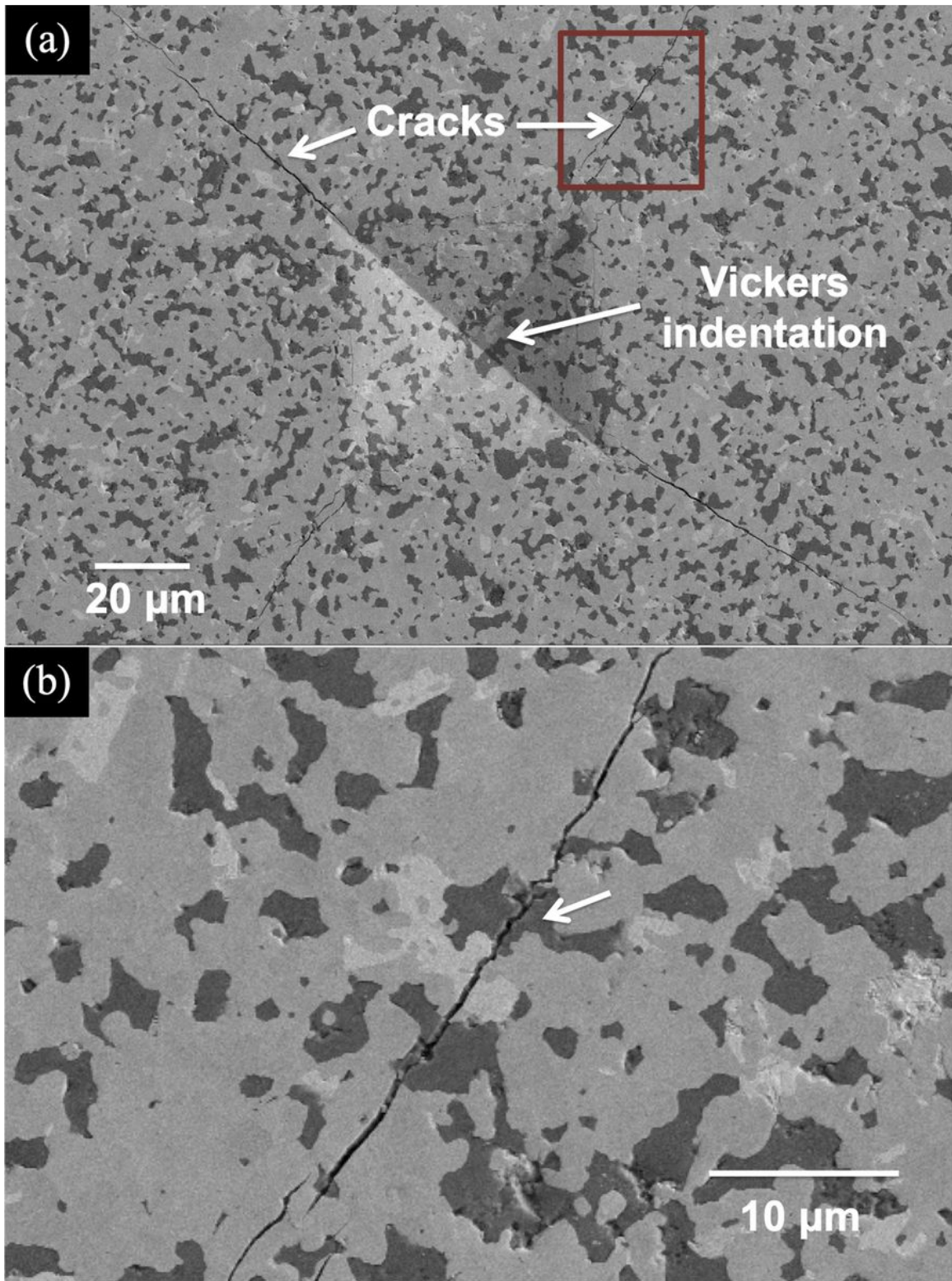


Figure 4

FESEM micrograph of SPSed (a) ZMSw20 and EDS mapping of (b) Zr, (c) Mo and (d) Si



**Figure 5**

Micrographs show (a) cracks are propagated from the corner of a Vickers indentation of ZMSw20 composite and (b) magnified view of the marked portion of figure (a).

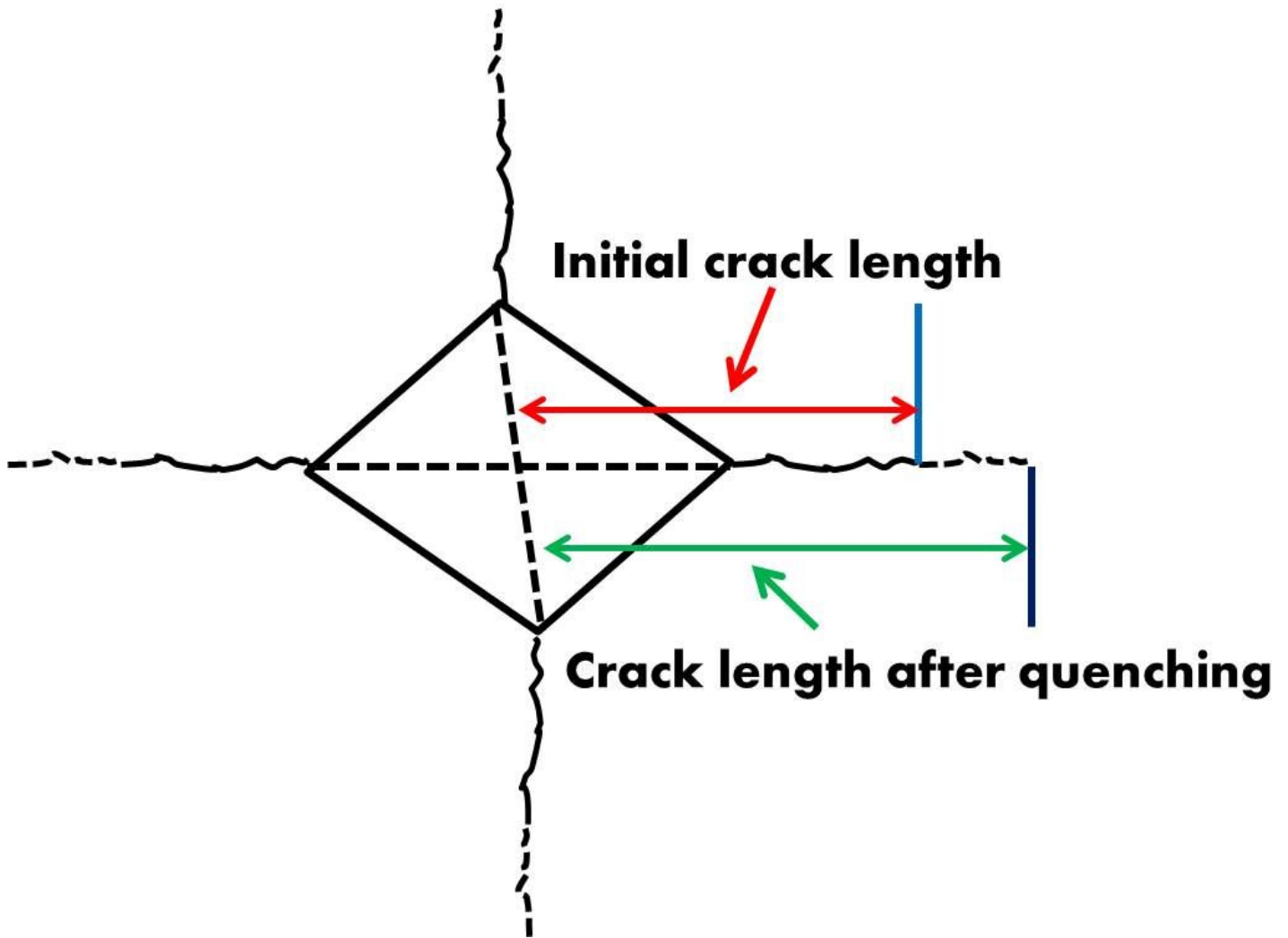


Figure 6

Schematic diagram showing cracks form at the corners and grow up after quenching.

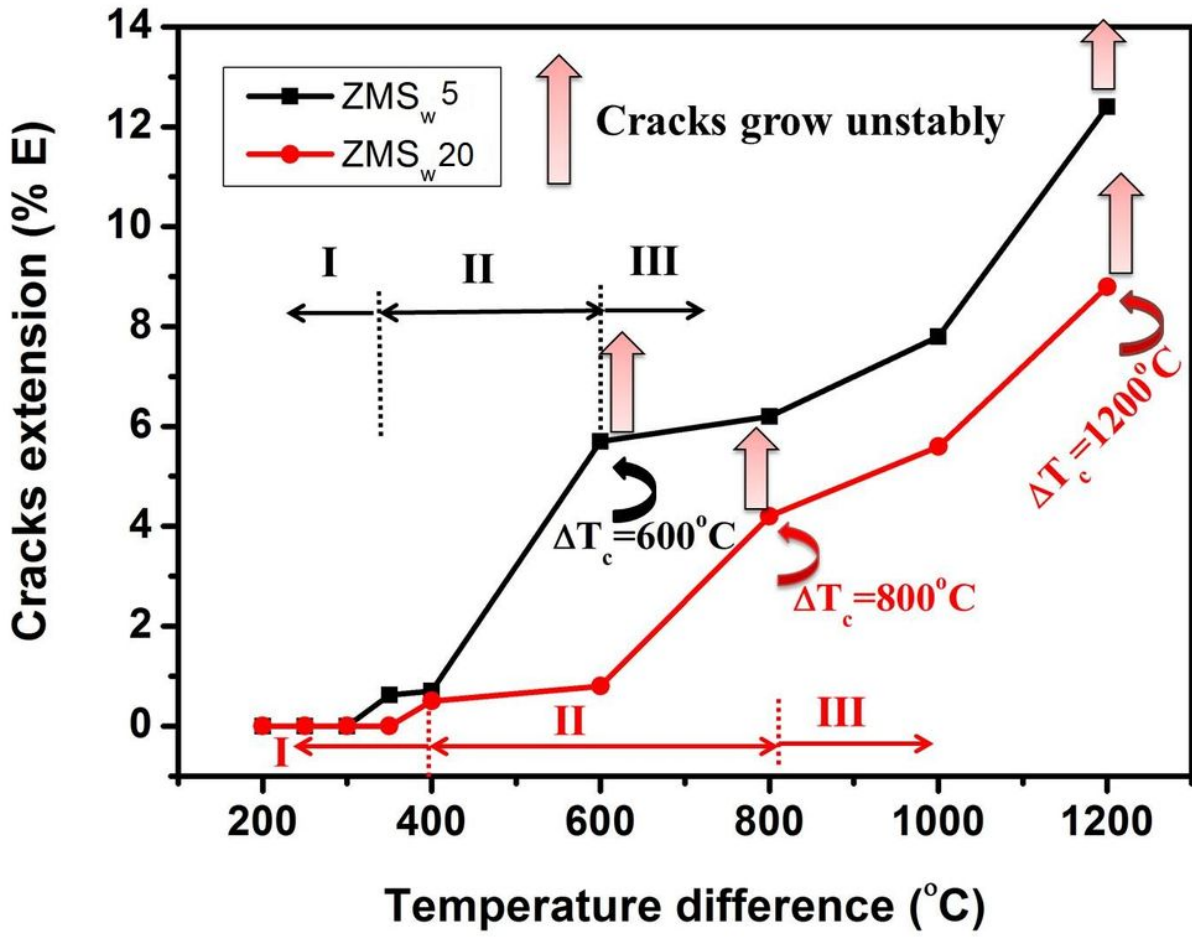


Figure 7

The percentage of crack extension after water quench at room temperature vs. quenching temperature differential for ZMSw5 and ZMSw20 composites.

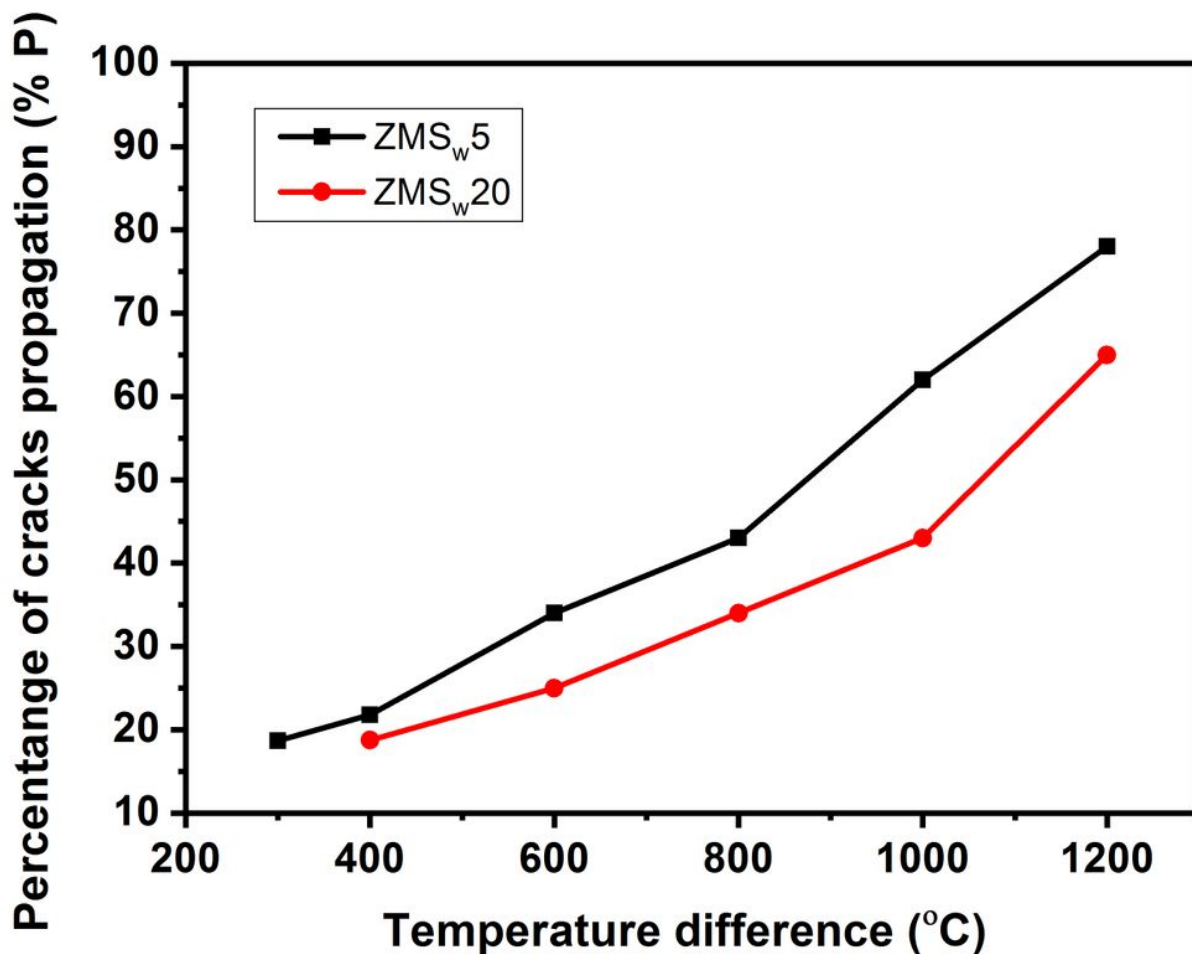


Figure 8

The percentage of crack propagation (% P) after water quench at room temperature vs. quenching temperature differential for ZMSw5 and ZMSw20 composites.

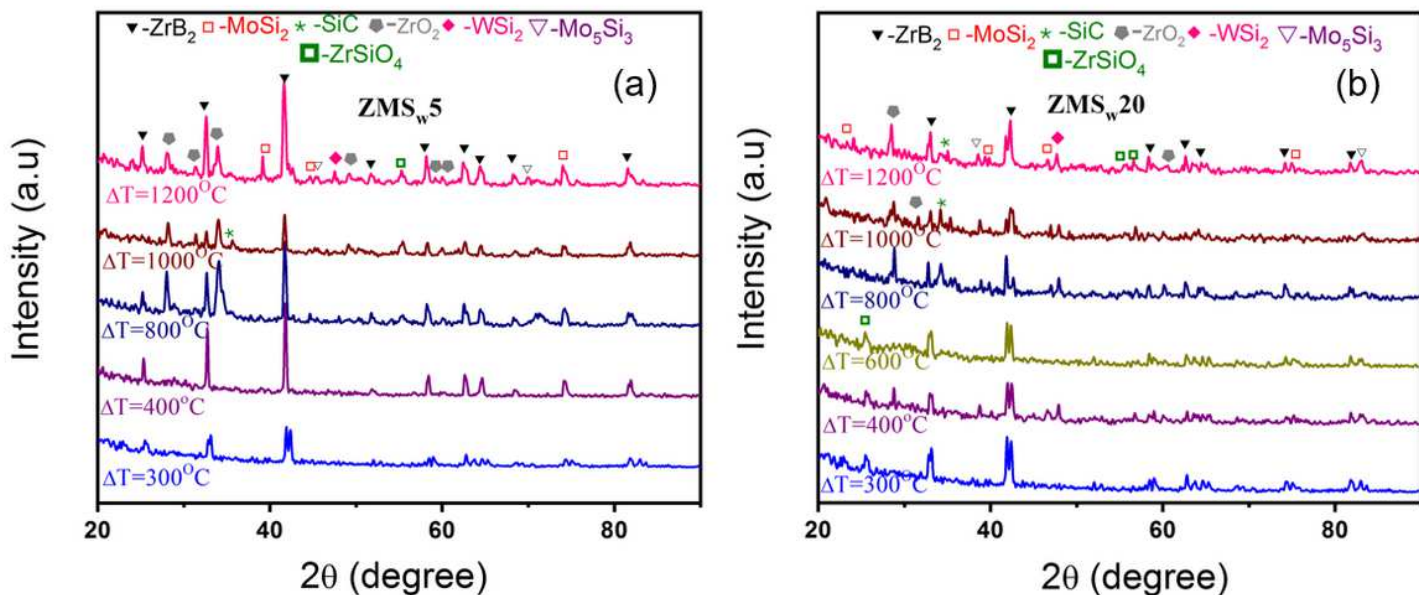


Figure 9

XRD spectrums of sample surface afterward thermal shock at different temperature differences: (a) ZMSw5 and (b) ZMSw20.

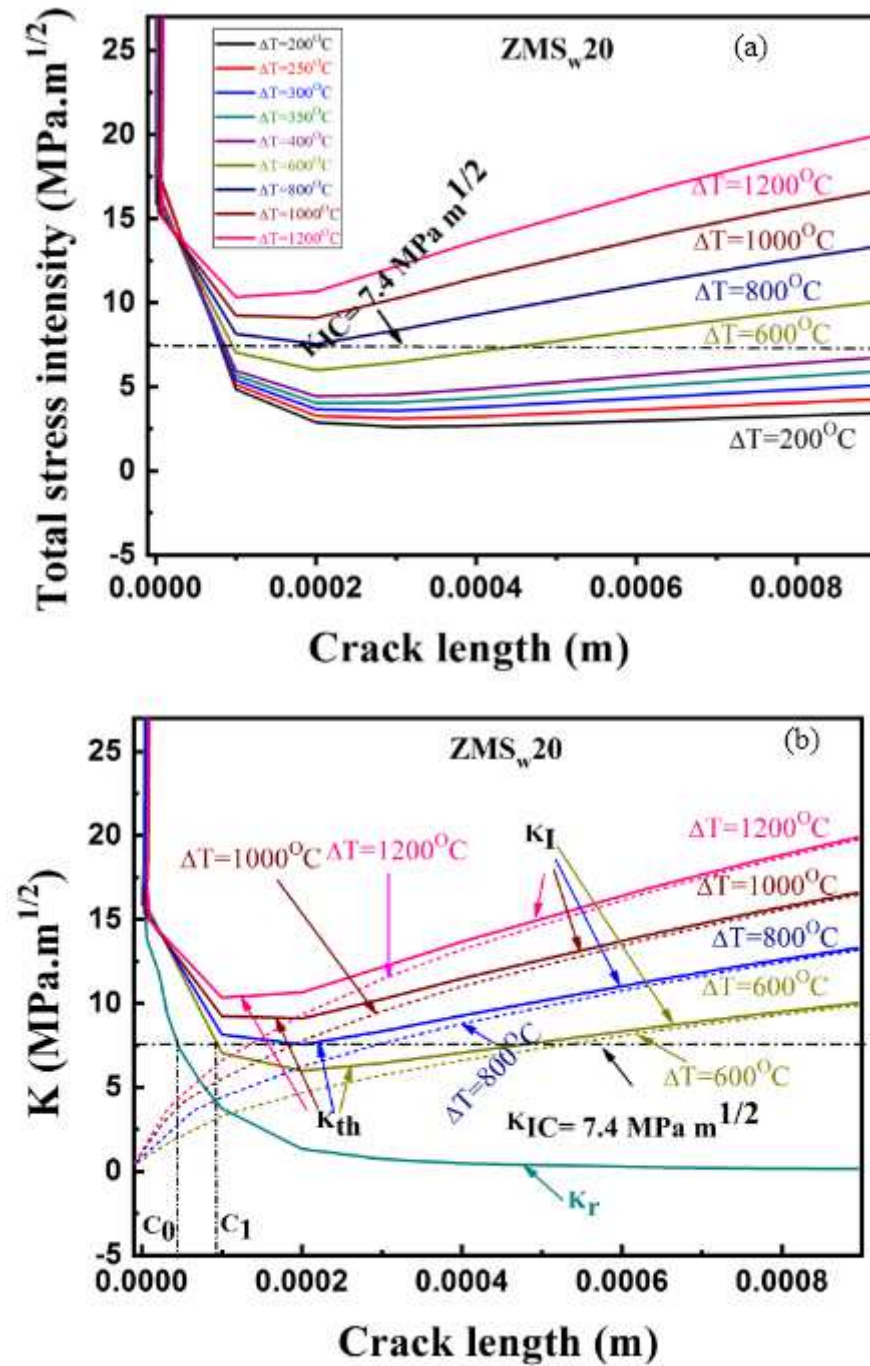


Figure 10

Total stress intensity with various  $\Delta T$  vs. of crack length and stress intensity with certain  $\Delta T$  of Vickers indentation cracks at the surface vs. indentation crack length after water quenching for ZMSw20 ceramics (a,b).

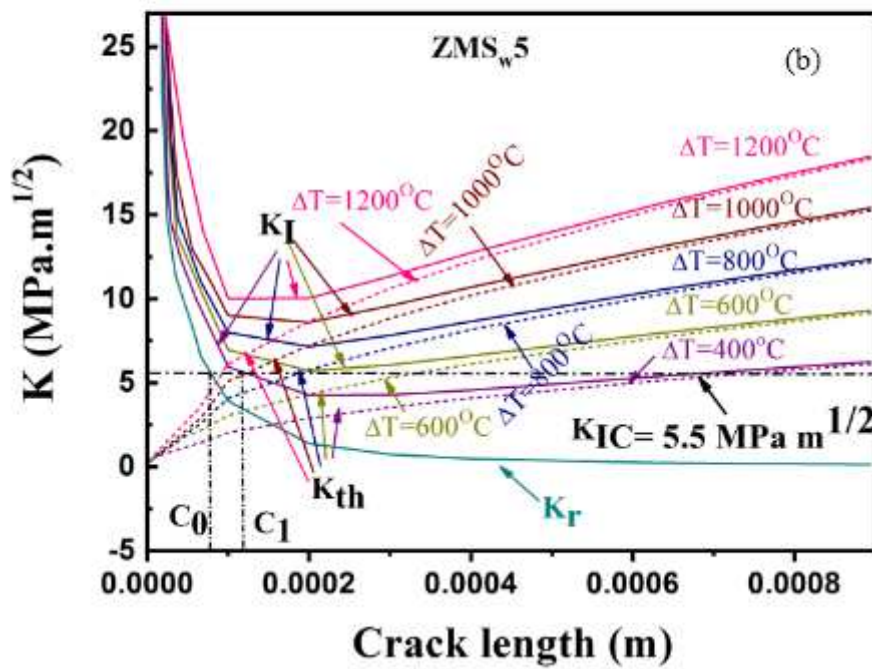
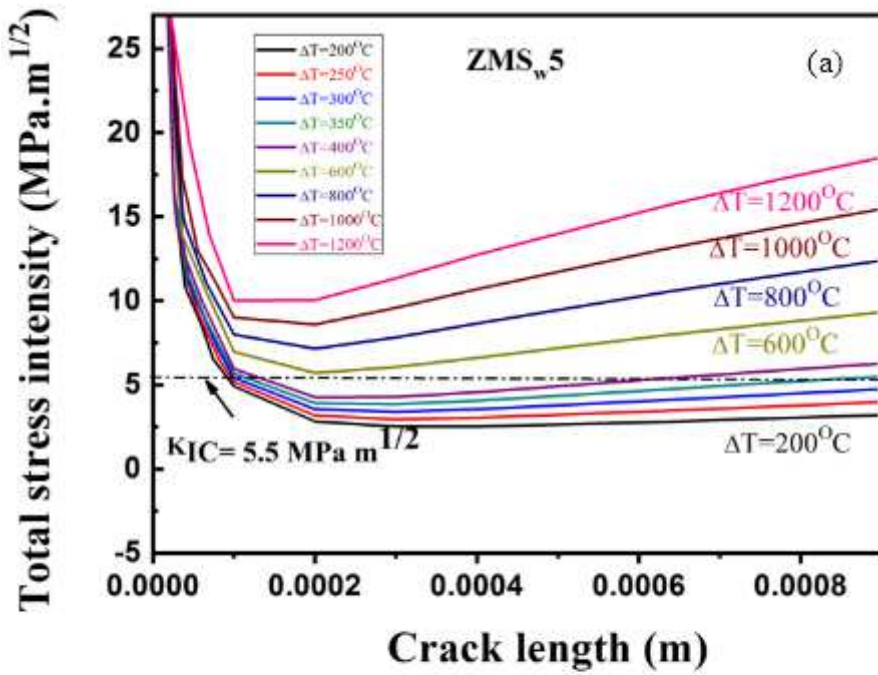


Figure 11

(a) Total stress intensity with various  $\Delta T$  vs. crack length and (b) stress intensity with certain  $\Delta T$  of Vickers indentation cracks at the surface vs. indentation crack length after water quenching for ZMSw5 ceramics.

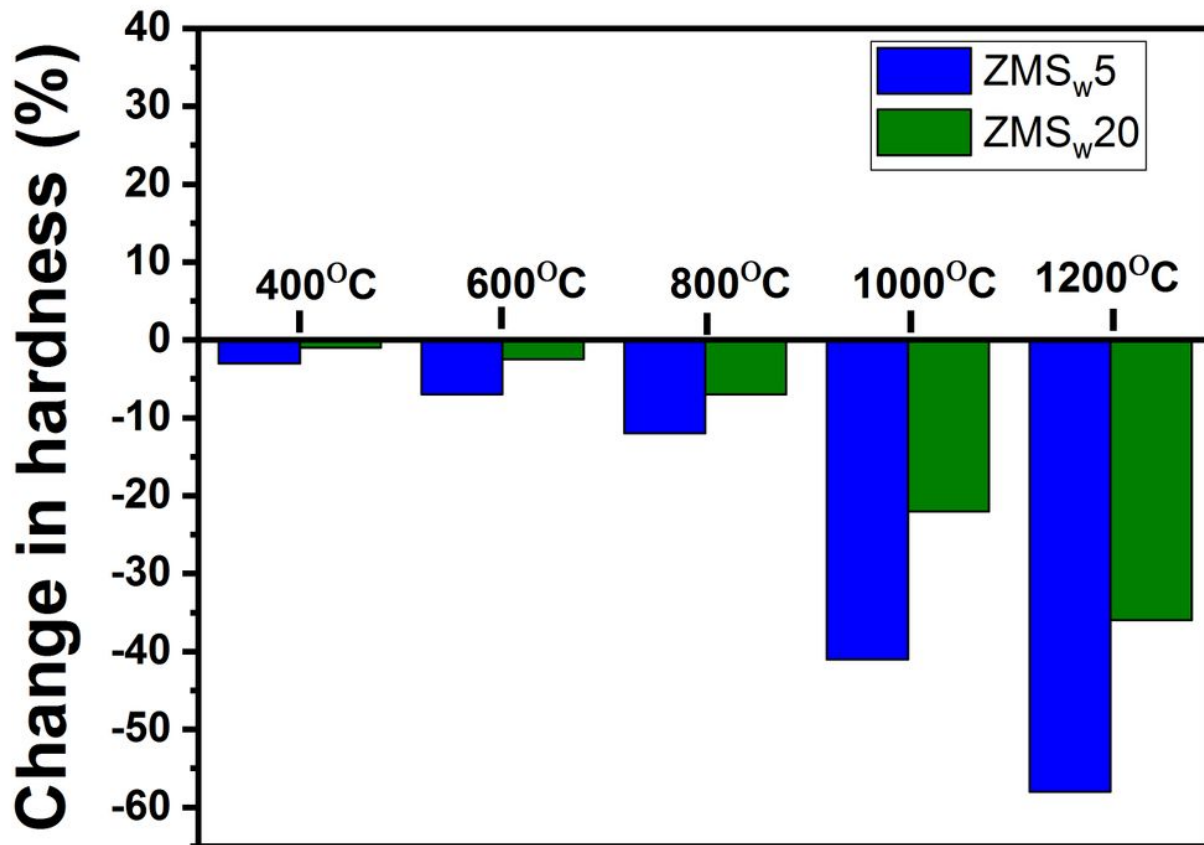


Figure 12

Bar chart displaying changes in hardness of the ZMSw composites due to thermal shock through at soaking various temperatures.